HAL
open science

Crustal-scale transcurrent fault development in a weak-layered crust from an integrated geophysical research: Carboneras Fault Zone, eastern Betic Cordillera, Spain

Antonio Pedrera, Flor de Lis Mancilla, Ana Ruiz-Constan, Jesus Galindo-Zaldivar, Jose Morales, Jorge Arzate, Carlos Marin-Lechado, Patricia Ruano, Luisa Buontempo, Farida Anahnah, et al.

To cite this version:

Antonio Pedrera, Flor de Lis Mancilla, Ana Ruiz-Constan, Jesus Galindo-Zaldivar, Jose Morales, et al.. Crustal-scale transcurrent fault development in a weak-layered crust from an integrated geophysical research: Carboneras Fault Zone, eastern Betic Cordillera, Spain. Geochemistry, Geophysics, Geosystems, 2010, 11, pp.Q12005. 10.1029/2010GC003274 . hal-00671024

HAL Id: hal-00671024

https://hal.science/hal-00671024v1

Submitted on 27 Sep 2021

HAL is a multi-disciplinary open access archive for the deposit and dissemination of scientific research documents, whether they are published or not. The documents may come from teaching and research institutions in France or abroad, or from public or private research centers.

L'archive ouverte pluridisciplinaire **HAL**, est destinée au dépôt et à la diffusion de documents scientifiques de niveau recherche, publiés ou non, émanant des établissements d'enseignement et de recherche français ou étrangers, des laboratoires publics ou privés.

Copyright

Geochemistry Geophysics Geosystems G3

Article
Volume 11, Number 12
11 December 2010
Q12005, doi:10.1029/2010GC003274
ISSN: 1525-2027

Published by AGU and the Geochemical Society

Crustal-scale transcurrent fault development in a weak-layered crust from an integrated geophysical research: Carboneras Fault Zone, eastern Betic Cordillera, Spain

Antonio Pedrera
Instituto Geológico y Minero de España, Rios Rosas 23, E-28003 Madrid, Spain (a.pedrera@igme.es)

Flor de Lis Mancilla
Instituto Andaluz de Geofísica, Universidad de Granada, Campus Universitario de Cartuja s/n, E-18071 Granada, Spain

Also at Departamento de Física Teórica y del Cosmos, Universidad de Granada, Campus de Fuentenueva s/n, E-18002 Granada, Spain

Ana Ruiz-Constán
Géosciences Montpellier, CNRS-Université Montpellier 2, Place E. Bataillon, F-34095 Montpellier CEDEX 5, France

Jesús Galindo-Zaldívar
Departamento de Geodinámica, Universidad de Granada, Campus Fuentenueva s/n, E-18002 Granada, Spain

Also at Instituto Andaluz de Ciencias de la Tierra, CSIC–Universidad de Granada, Campus Fuentenueva s/n, E-18002 Granada, Spain

José Morales
Instituto Andaluz de Geofísica, Universidad de Granada, Campus Universitario de Cartuja s/n, E-18071 Granada, Spain

Also at Departamento de Física Teórica y del Cosmos, Universidad de Granada, Campus de Fuentenueva s/n, E-18002 Granada, Spain

Jorge Arzate
Centro de Geociencias, Universidad Nacional Autónoma de México, Campus Juriquilla, 1-742 Querétaro, Mexico

Carlos Marín-Lechado
Instituto Geológico y Minero de España, Rios Rosas 23, E-28003 Madrid, Spain

Patricia Ruano
Departamento de Geodinámica, Universidad de Granada, Campus Fuentenueva s/n, E-18002 Granada, Spain

Also at Instituto Andaluz de Ciencias de la Tierra, CSIC–Universidad de Granada, Campus Fuentenueva s/n, E-18002 Granada, Spain

Copyright 2010 by the American Geophysical Union

Luisa Buontempo
Instituto Andaluz de Geofísica, Universidad de Granada, Campus Universitario de Cartuja s/n, E-18071 Granada, Spain

Farida Anahnah
Departamento de Geodinámica, Universidad de Granada, Campus Fuentenueva s/n, E-18002 Granada, Spain

Daniel Stich
Instituto Andaluz de Geofísica, Universidad de Granada, Campus Universitario de Cartuja s/n, E-18071 Granada, Spain

Also at Departamento de Física Teórica y del Cosmos, Universidad de Granada, Campus de Fuentenueva s/n, E-18002 Granada, Spain

[1] New magnetotelluric and receiver transfer function studies provide insights from the upper to the lower crust of the eastern Betic Cordillera, which is deformed by large folds, normal faults, and a major transcurrent left-lateral fault, the Carboneras Fault Zone (CFZ). Receiver function analysis determines a NNW dipping Moho reaching 20° that increases in depth, from 20 km south of the CFZ up to 34 km in the Sierra de Los Filabres. In addition, seismic discontinuities determined in the upper crust are interpreted as major contacts between metamorphic complexes that are detached and folded. The MT inversion model reveals a conductive zone, also representing a crustal seismic discontinuity, associated with the Alpujárride/Nevado-Filábride contact and fitting the N vergent geometry of the Sierra Alhamilla antiform. A small flexure at Moho coincides with the CFZ, as revealed by the Bouguer anomaly trend, in agreement with the receiver function results. Moreover, the Bahr strike and tipper angle at the stations placed closest to the CFZ clearly reveal the continuity of the CFZ at least down to approximately 15 km in depth, crossing all the detected crustal discontinuities up to the Moho. The lack of a clear Moho offset associated with the Carboneras Fault supports the idea that some large strike-slip faults tend to accommodate the deformation by a broadening fault zone at lower crustal levels. Its nucleation could occur at the base of a thin crust, where melting processes critically reduced the lithospheric strength during the late Miocene, to then propagate upward, reaching the topographic surface. Northward, the lithosphere comprised moderately larger strength, and the crustal discontinuities favored the development of larger folds with kilometric amplitude instead of strike-slip faults since the late Miocene.

Components: 12,000 words, 13 figures, 2 tables.

Keywords: magnetotelluric data; receiver function; strike-slip fault; folds; crustal detachments.

Index Terms: 8004 Structural Geology: Dynamics and mechanics of faulting (8118); 8002 Structural Geology: Continental neotectonics (8107); 8031 Structural Geology: Rheology: crust and lithosphere (8159).

Received 22 June 2010; **Revised** 6 October 2010; **Accepted** 18 October 2010; **Published** 11 December 2010.

Pedrera, A., et al. (2010), Crustal-scale transcurrent fault development in a weak-layered crust from an integrated geophysical research: Carboneras Fault Zone, eastern Betic Cordillera, Spain, *Geochem. Geophys. Geosyst.*, *11*, Q12005, doi:10.1029/2010GC003274.

1. Introduction

[2] The crustal nature determines different features of accommodation of the strain during tectonic deformation. Under the same stress field, the tectonic structures generated in strong homogeneous crusts are quite different from the structures developed in weak-layered crusts [*Butler and Mazzoli*, 2006]. The thermomechanical structure of the crust controls the behavior of major strike-slip faults and their continuity at depth. Therefore, while transcurrent faults that affect homogeneous crusts and/or crosscut across plate boundaries tend to extend through all the crust, transcurrent faults that deform layered crusts generally interact with crustal detachment zones [*Sibson*, 1977; *Hanmer*, 1988; *Lemiszki and Brown*, 1988; *Roy and Royden*, 2000;

Wilson et al., 2004]. Geophysical studies help constrain the relationship between strain distribution and the rheology at a crustal scale. In weak-layered crusts, detachments and Moho location may be detected using seismological techniques and highlighted as major seismic wave velocity discontinuities [*Doll et al.*, 1996; *Hole et al.*, 2000; *Zhu and Kanamori*, 2000; *Zhu*, 2002]. Meanwhile, electromagnetic methods have been applied to characterize the electrical properties of the crust, which are closely linked to its lithology and fluid content [*Bertrand et al.*, 2009; *Yoshimura et al.*, 2009].

[3] The Betic and Rif Cordilleras are located along the convergent boundary between the African and Eurasian plates. Many geological and geophysical studies have focused on the identification of recent structures in order to establish the mechanisms responsible for the orogen's tectonic evolution. Since the upper Miocene, these major tectonic structures show a heterogeneous distribution, dominated by fold and normal faults in the central Betics, and by strike-slip faults that interact with folds and normal faults in the eastern sector of the cordillera. Although some of the most important features of the crust have been assessed at a regional scale on the basis of geophysical research, a number of specific questions remain unanswered.

[4] The aim of this work is to characterize the structure of the crust in a sector of the eastern Betic Cordillera deformed by folds, numerous normal faults, and a major strike-slip fault zone known as the Carboneras Fault Zone (CFZ). The continuity of the CFZ from the upper to the lower crust and, therefore, the strain distribution along the fault zone are matters that remain unclear. While magnetotelluric data and structural analysis of the outcropping tectonic structures are used to constrain the deformation style of the upper crust, seismic receiver function analysis provides us with new insights regarding the middle and lower crust of this sector of the Cordillera, including Moho depth variations and crustal heterogeneities. Our study enriches discussion of the possible models of crustal-scale transcurrent fault development.

2. Geological Setting

[5] The Betic Cordillera represents the northern branch of the Gibraltar Arc, which constituted the western end of the Mediterranean Alpine Chain developed along the African-European plate boundary. Plate kinematic reconstructions suggest that this plate boundary experienced continuous N-S to NW-SE shortening during the Neogene [*Dewey et al.*, 1989; *Srivastava et al.*, 1990; *Müller and Roest*, 1992; *Mazzoli and Helman*, 1994; *Rosenbaum et al.*, 2002]. The present-day plate boundary is very diffuse and one or more additional microplates are commonly invoked [*Fadil et al.*, 2006]. Three main geological domains compose the Betic Cordillera: the External Zones formed by Mesozoic and Cenozoic sedimentary rocks, the Flysch Units that are formed by Cretaceous to Miocene deep water flysches, and the Internal Zones made up of allochthonous tectonic nappes, which extensively include largely metamorphosed Paleozoic and Mesozoic rocks (Figure 1). Thrust-and-fold successions deformed the External Zones and the Flysch Units during the Latest Oligocene-Early to Middle Miocene, associated with the westward drift of the Internal Zones [*Balanyá and García-Dueñas*, 1987; *Crespo-Blanc and Campos*, 2001; *Luján et al.*, 2003]. The Internal Zones comprise three main tectonic complexes that have recorded an intense deformation history: (from bottom to top) the Nevado-Filábride, the Alpujárride and the Maláguide complexes [*Blumenthal*, 1927; *Van Bemmelen*, 1927; *Egeler*, 1963]. They are separated by low-angle normal faults that were active during the Early and Middle Miocene, recording a progressive ductile to brittle extension [*Aldaya et al.*, 1984; *García-Dueñas et al.*, 1988; *Galindo-Zaldívar et al.*, 1989; *Platt and Vissers*, 1989]. The westward shortening of the External Zones, the driving extension and exhumation of the hinterland of the orogen, and the Alboran Basin development were all probably related to subduction and slab rollback of the African crust during the Early and Middle Miocene [*Royden*, 1993; *Lonergan and White*, 1997].

[6] The relief of the Internal Zones of the Betic Cordillera, developed since the Late Miocene, is in turn related to the slow convergence between the European and the African plates. In this shortening framework, antiforms gave rise to elongated mountains, whereas synforms favored the development of elongated depressions between these mountain ranges. The folds interact with normal faults of variable scale that occasionally have associated asymmetrical Late Miocene sedimentary basins (Figure 1). Moreover, the eastern part of the Betic Cordillera is affected by a fault system characterized by large transcurrent left-lateral faults such as the Alhama de Murcia, Palomares and Carboneras faults; this fault system continues across the Alboran Sea and the northern Rif Cordillera across the

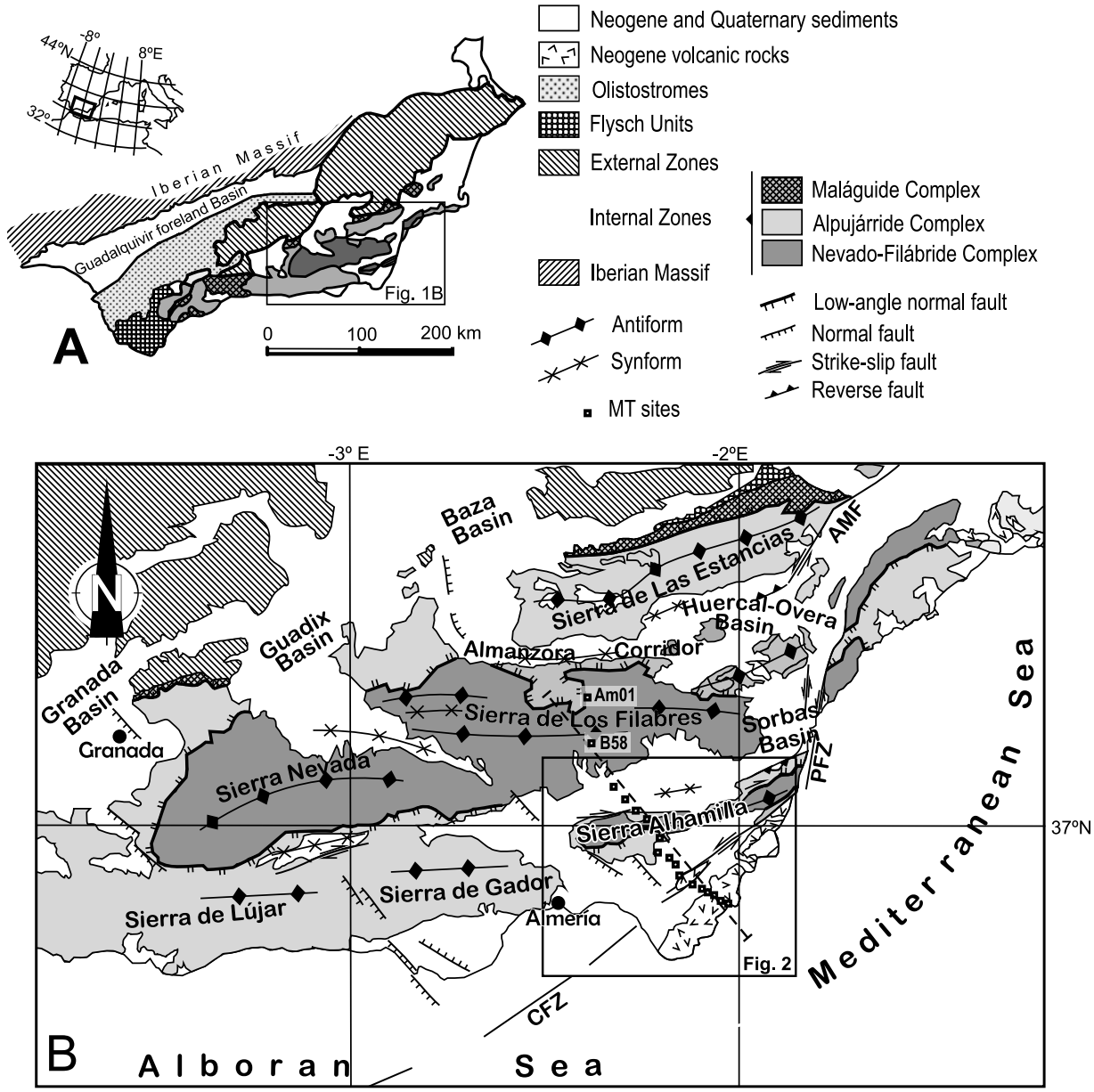

Figure 1. (a) Geological map of the Betic Cordillera and (b) enlarged geological map of the southeastern Betic Cordillera with the location of the MT profile.

Trans-Alboran Shear Zone [*De Larouzière et al.*, 1988].

[7] The location of the transcurrent fault coincides with the occurrence of Middle Miocene to Pleistocene volcanic rocks cropping out in a roughly NE-SW trending band, extending from southeastern Spain through the eastern Alboran Sea, into northeastern Morocco [*Duggen et al.*, 2008]. The studied area comprises the Late Miocene Tabernas and Níjar sedimentary basins, which are separated by the Sierra Alhamilla and the Sierra Cabrera antiforms and the coastal stratovolcanic complex of Cabo de Gata (Figure 2). The Carboneras Fault Zone (CFZ) is the largest tectonic structure in the studied area, coexisting with widespread NW-SE high dipping normal faults that have been active since the Late Miocene.

2.1. Carboneras Fault Zone

[8] The CFZ is a major regional left-lateral fault with tens of kilometers offset that extends onshore across the Almería-Carboneras Basin and continues offshore through the Almería Gulf with a NE-SW direction [*Bousquet and Montenat*, 1974;

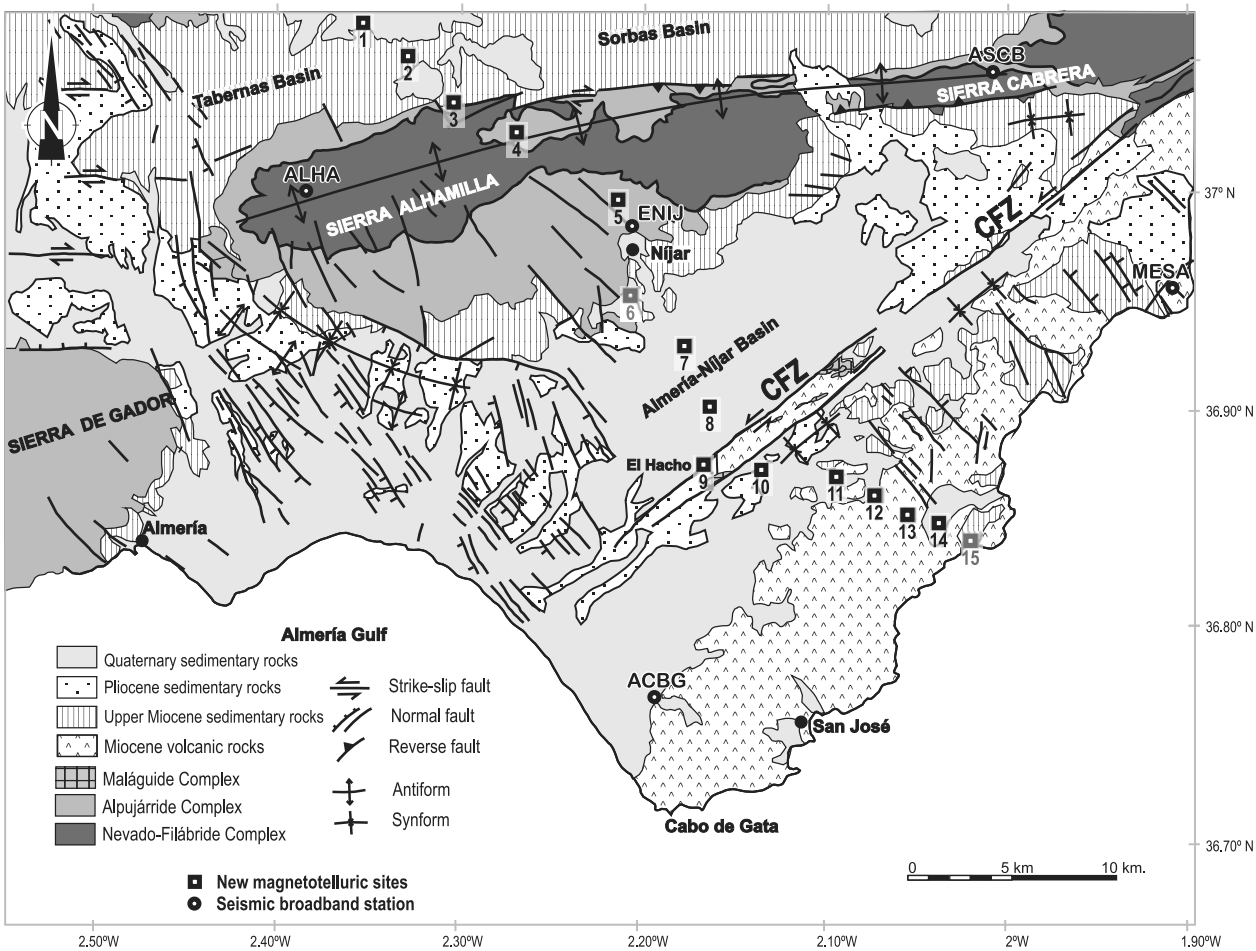

Figure 2. Geological map of the studied area showing the recent tectonic structures, the position of the new magnetotelluric sites, and the seismic stations.

Van de Poel, 1991; *Gràcia et al.*, 2006]. Although a main left-lateral shear is deduced from the outcropping fault gouge, a transpressive component is also inferred from the associated positive relief across La Serrata ridge and its offshore continuation through the Almería Gulf. The CFZ mainly involves Late Miocene sediments and Alpujárride, Maláguide and volcanic basement rocks, constituting a fault gouge up to hundreds of meters thick in some places that is delimited by two main subparallel fault planes (Figure 2). The activity of the CFZ started between the Middle Miocene [*Ott d'Estevou and Montenat*, 1985; *Keller et al.*, 1995; *Scotney et al.*, 2000; *Faulkner et al.*, 2008] and the Late Miocene [*Montenat and Ott d'Estevou*, 1990]. It is widely accepted that its activity during the Late Miocene was simultaneous with deep water sedimentation and partially coincided with volcanic activity [*Montenat and Ott d'Estevou*, 1990]. Nevertheless, its continuity and its kinematics since the Pliocene are under debate [*Rutter et al.*, 1986; *Faulkner et al.*, 2003, 2008; *Pedrera et al.*, 2006; *Moreno et al.*, 2007].

[9] Several geophysical studies of the CFZ have attempted to establish its continuity at depth and the character of the crust on either side of the fault. Deep seismic refraction research [*Working Group for Deep Seismic Sounding in the Alboran Sea, 1974*, 1978] suggests the presence of different crustal types separated by the Carboneras Fault [*Banda and Ansorge*, 1980; *Banda et al.*, 1993]. A gravimetric and magnetic study constrained the basement offset linked to the CFZ and the location of volcanic rocks on both sides of the CFZ [*Pedrera et al.*, 2006].

2.2. Sierra Alhamilla Antiform

[10] The highest reliefs in the area are linked to culminations on the hinge line of the Sierra Alhamilla open antiform, which shows an ENE-WSW

orientation, 25 km in length, 10 km of maximum amplitude, and reaches more than 1300 m in height. The Early Tortonian-Serravallian conglomerates and the Late Tortonian sediments that surround the range are folded, allowing infer the fold geometry and the age of the deformation. The Late Tortonian rocks dip 20° in the southern slopes, yet are vertical or even overturned in the northern slopes as a consequence of the northward fold vergence [*Weijermars et al.*, 1985]. The antiform growth favored the elevation and the erosion of the Alpujárride and Nevado-Filábride metamorphic rocks that constitute the basement of the adjacent sedimentary basins. Therefore, the range represents an exceptional outcrop for characterizing the Lower and Middle Miocene ductile to brittle extensional tectonic evolution of the metamorphic rocks [*Platt and Vissers*, 1989; *Martínez-Martínez and Azañón*, 1997]. The Sierra Alhamilla antiform development is coeval with a main E-W oriented high-angle right-lateral to reverse fault that deforms its northern border (Figure 2).

3. Previous Geophysical Research

[11] Several magnetotelluric studies have been performed in the central and eastern Betic Cordillera. *Pous et al.* [1999] performed a 2-D model along a NW-SE oriented profile that extends from the Guadalquivir foreland basin, crossing the Cordillera, as far as the Sierra Alhamilla, in the Internal Zones. Their results show a deep conductive body in the lower crust below the Internal Zones, which is interpreted as partial melting of a thickened continental crust. Northward of the studied area, across the Sierra de Los Filabres and the Almanzora Corridor, *Pedrera et al.* [2009] carried out a multidisciplinary study of the crustal structures from broadband magnetotelluric, gravity, and magnetic data, revealing a conductive/magnetic body under the Sierra de Los Filabres possibly related to basic igneous rocks. The geometry of this conductor was laterally constrained by *Martí et al.* [2009], who computed a regional 3-D forward model with a broad sites distribution, and interpreted the conductive body as part of an ancient oceanic crust.

[12] Crustal geophysical data including Moho information are very scarce in the eastern Betic Cordillera. Bouguer anomaly progressively decreases to the NNW, from 50 mGal close to the coast line to −70 mGal in the Sierra de Los Filabres, and shows dip variations [*Instituto Geográfico Nacional* (*IGN*), 1975]. Deep seismic refraction profiles were undertaken in the Betic Cordillera and the Alboran Sea during the seventies [*Working Group for Deep Seismic Sounding in the Albora Sea, 1974*, 1978]. Interpretations of the profiles located in the Betic Cordillera suggest the presence of different crustal layers separated by the CFZ [*Banda and Ansorge*, 1980; *Banda et al.*, 1993]. They moreover suggest that the crust eastward of the fault system is faster and thinner than that found to the west (~23 km thick and Vp = 6.3 km/s versus ~30 km thick and Vp = 6.1 km/s). The refraction Moho detected beneath the Sierra de Los Filabres is located between 30 and 35 km. Deep reflection seismic profiles ESCI-BETICAS and ESCI-ALBORAN helped assess the deep structure of the Betic Cordillera and its transition to the Alboran crust. The ESCIBETICAS-2, crossing both Sierra Nevada and Sierra de Los Filabres, shows sectors with subhorizontal crustal reflectors whose boundaries could correspond to detachment levels at a depth of 20 km [*García-Dueñas et al.*, 1994; *Galindo-Zaldívar et al.*, 1997]. The transition between a ~15 km thick continental crust of the Alboran Sea and a ~6 km thick oceanic crust of the Algerian basin has been recently characterized by reprocessing the E-W oriented ESCI-Alboran deep reflection seismic profile [*Booth-Rea et al.*, 2007].

4. Magnetotelluric Research

[13] New broadband magnetotelluric data acquired along a transect crossing the large Sierra Alhamilla antiform and the CFZ, in the southeastern part of the Betic Cordillera, contribute to characterization of the electrical structure of the upper crust while providing insight about the development of kilometric amplitude folds and crustal-scale transcurrent faults in these weak-layered crusts.

4.1. Sierra Alhamilla–CFZ Profile

[14] The new MT survey was performed along a NW-SE line roughly perpendicular to the regional geological strike (Figures 1 and 2). We collected 15 new measurements during May 2009 and we used two sites (Am01 and B58) from a previous survey carried out to the north during the summers of 2005 and 2006 [*Pedrera et al.*, 2009]. All the sites were obtained using a Metronix ADU06, covering a period band from 0.0001 to 100 s. The sites planned to install the magnetotelluric stations were very scarce in the northern part of the Almería-Níjar Basin because is crossed by high-voltage power lines. Data were processed using a robust cascade decimation algorithm [*Wight and Bostick*,

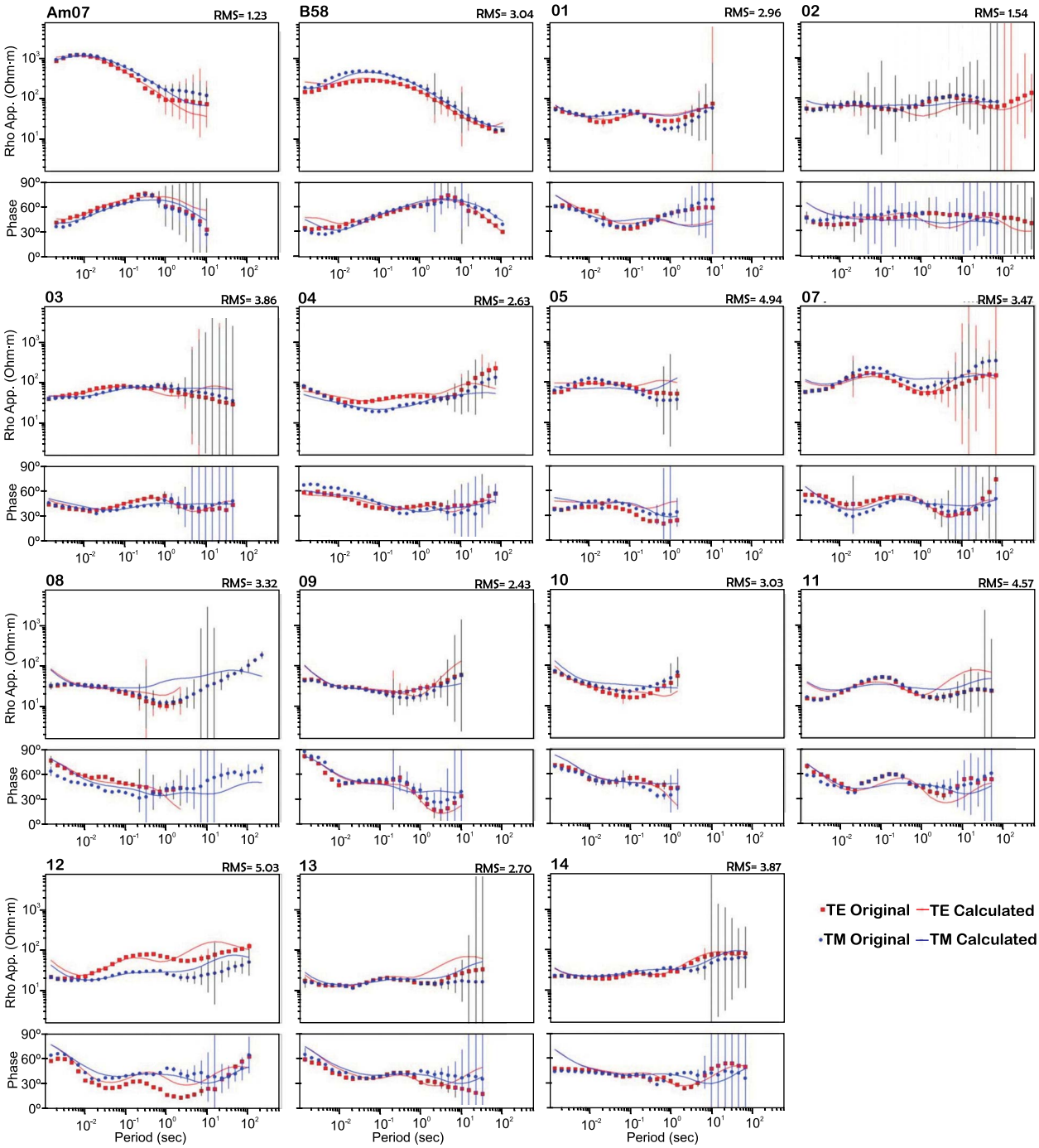

Figure 3. Magnetotelluric resistivity (Rho App.) and phase curves and model responses.

1980] and showed good quality overall, but which considerably decreases between 50 to 100 s (Figure 3).

4.2. Dimensionality and Geoelectric Strike

[15] The dimensionality and geoelectric strike, defined as the horizontal direction along the conductivity is constant in a two-dimensional electrical Earth [*Simpson and Bahr*, 2005], were investigated using induction arrows, phase tensor analysis [*Caldwell et al.*, 2004], and Bahr's phase consistent strike method [*Simpson and Bahr*, 2005]. Phase tensor ellipsoids show a nearly constant N-S direction of the major principal axis from 0.001 to 0.1 s, then changing to the NE-SW from 0.1 to 100 s, revealing a mostly two-dimensional conductivity

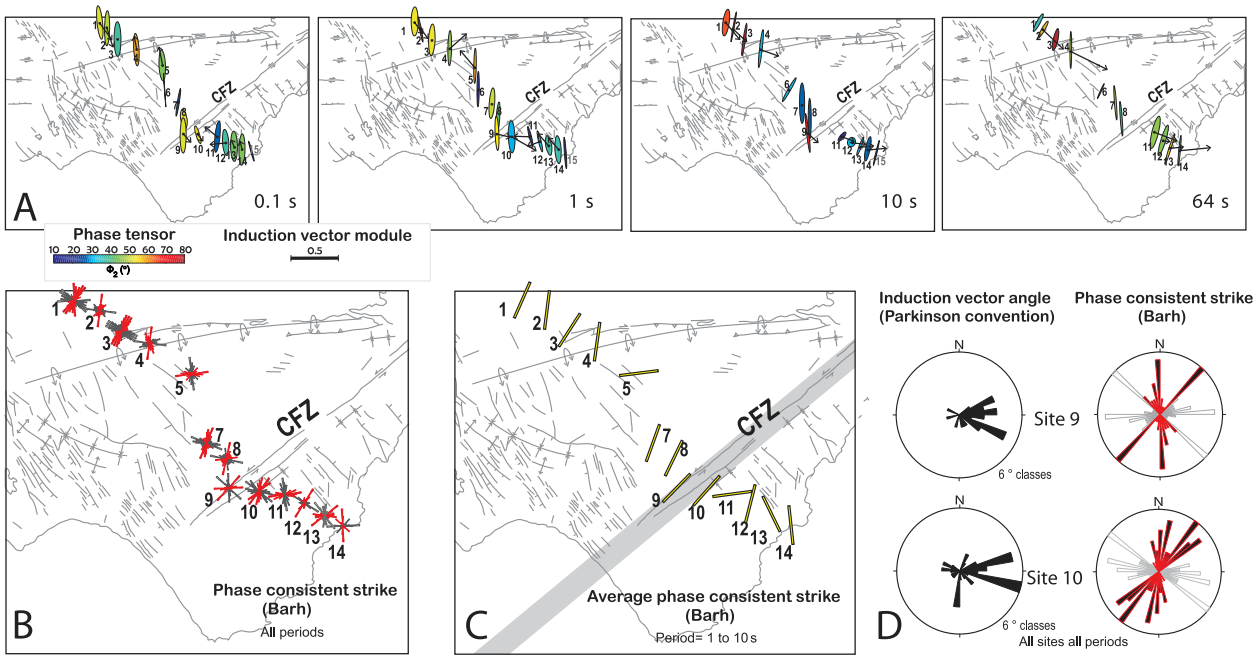

Figure 4. Dimensionality analysis of the MT data. (a) Phase sensitive strike and induction vector (Parkinson convention) obtained at periods of 0.1, 1, 10, and 64 s. (b) Phase consistent strike (Bahr) results including all periods. (c) Average phase consistent strike (Bahr) results between periods of 1 and 10 s. (d) Phase sensitive strike and induction vector (Parkinson convention) in the stations 9 and 10, placed close to the CFZ. Note that they have a geoelectrical strike parallel to and tipper angle orthogonal to the fault zone.

structure (Figure 4a). The sites with a reliable tipper angle reveal a dominant N145°E direction of the induction vectors, orthogonal to the main geological structures, particularly to the CFZ. Analysis of the strike angle was performed [*Simpson and Bahr*, 2005] for each MT station, giving a general NNE-SSW to ENE-WSW direction for all the measured period range (Figure 4b). However, when the strike is estimated for a limited period range, say 1–10 s, the average strike is more stable and correlates reasonable well with the CFZ strike. The Bahr strike obtained at sites 9 and 10 is parallel to the CFZ (Figure 4c), indicating that the preferred flow direction of the electrical currents is related to anisotropic fabrics linked to the fault zone. In addition, induction arrows obtained in stations 9 and 10 are clearly orthogonal to the CFZ (Figure 4d), coinciding with the Bahr strike results. The maximum depth investigated in a magnetotelluric sounding, skin depth (δ), is related to frequency and resistivity of the subsurface rocks ($\delta \sim 0.5$ (resistivity/frequency)$^{0.5}$, where skin depth is expressed in kilometers, resistivity in Ω m and frequency in hertz). The estimated penetration depth at station 9 suggests continuity of the CFZ at least down to 15 km. Notwithstanding the 3-D behavior at specific sectors, the well-defined phase tensor ellipsoid orientation, the strike direction, and the induction vector consistency at the modeled periods validate 2-D analysis. Before 2-D modeling, a study of the ocean effect was performed in order to determine the period range in which the ocean did not influence the data. A synthetic MT 3-D modeling using the MT3FWD code [*Mackie et al.*, 1994] demonstrates that the studied frequencies are weak affected by the presence of a lateral conductive seawater. Only the data from the station 15, placed in the coast, do seem to be distorted by the conductive ocean water and was not included in the modeling.

4.3. Resistivity Inversion Models

[16] The TE and TM modes, resistivity and phase, were inverted using the 2-D finite difference inversion code of *Rodi and Mackie* [2001]. The inversion started with a homogeneous intermediate resistivity of 100 Ω m and with a regular lateral cell size, that increases with depth. Regarding the dimensionality analysis results, two inversions were performed: without rotation according to the phase tensor ellipsoids between 0.001 to 0.1 s, and rotating the impedance according to the induction vector, and phase tensor ellipsoids between 0.1 to 100 s. We obtained quite similar results; only slight

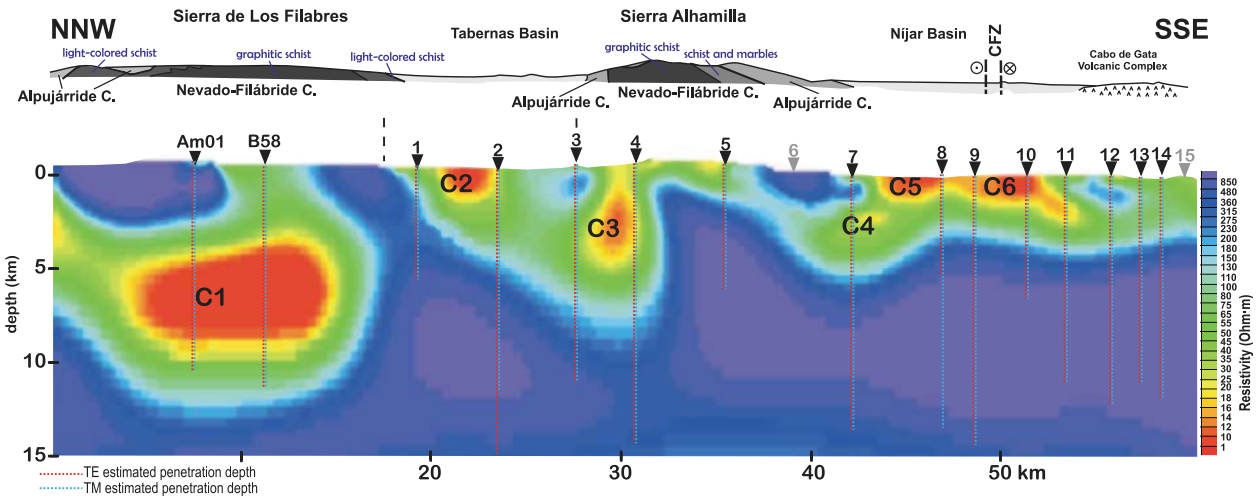

Figure 5. Magnetotelluric 2-D inversion model. The location of the 17 MT sites is marked; the new sites 1–15 were acquired during May 2009, and sites B58 and Am01 were measured during the summers of 2005 and 2006, respectively. The conductors are numbered (C1–C6).

horizontal displacements in some of the conductive bodies were detected. The smoothing factor τ selected during the inversion was 3 and the floor standard deviation error considered for resistivity and phases of both polarization modes was 5.0%. The resistivity image obtained from the −35° rotated model shows the best misfit (RMS = 3.16) and the best geological correlation with the outcropping structures (Figures 5 and 6). Figure 5 shows the results of the selected inversion model. The northern part of the model is characterized by a conductor (C1, ~0.5 Ω m) that extends from 4 to 9 km between stations Am01 and B58, beneath the Sierra de Los Filabres. A conductive body (C2, ~1 Ω m) is situated between stations 1 and 2, extending from the topographic surface to 1 km depth. In the central part of the model, between stations 4 and 5, a resistive body (~500 Ω m) emerges close to the topographic surface, and is surrounded by a conductive zone that discontinuously extends southward below the Níjar basin (C4, ~20 Ω m) and northward bordering the Tabernas basin (C3, ~12 Ω m). Between sites 7 and 10, a ~1 km thick conductive zone (C5 and C6, ~5 Ω m) coincides with the location of the Almería-Níjar basin and the CFZ. To test the robustness and resolution of the obtained electrical anomalous bodies, a verification was performed by omitting some sites, varying the mesh dimensions, and replacing the conductor by intermediate bodies of 100 Ω m and then running the forward model response to estimate their influence. The RMS error considerably increases after removal of each conductor, thereby revealing the consistency of the obtained model (Figure 7).

5. Seismic Receiver Function Analysis

5.1. Data and Methodology

[17] We calculate P receiver functions from teleseismic events recorded by 5 seismic broadband stations deployed around the CFZ (Figure 2) by the Instituto Andaluz de Geofisica (IAG, http://www.ugr.es/iag). Station recording times vary from one year (ENIJ) to more than four years (ASCB), producing disparity in the amount of available receiver functions from 26 (ENIJ) to 115 (ASCB). The P receiver functions are time series containing P-to-S (Ps) converted and multiple-reverberated phases generated at seismic discontinuities beneath the recording stations [*Langston*, 1979]. Receiver functions have been obtained by deconvolving, in the time window corresponding to the teleseismic P wave coda, the vertical component of each event from the corresponding horizontal components using an iterative time domain deconvolution method [*Ligorria and Ammon*, 1999]. The deconvolved time series were low-pass filtered below 1.2 Hz to minimize the presence of random noise. The deconvolution process removes the effect of the source, the instrument response from the waveforms, and the common path before the conversion, keeping the information of the local structure below the seismic station [*Langston*, 1979]. Previous to deconvolution, we rotated the vertical, radial and transversal components (ZRT)

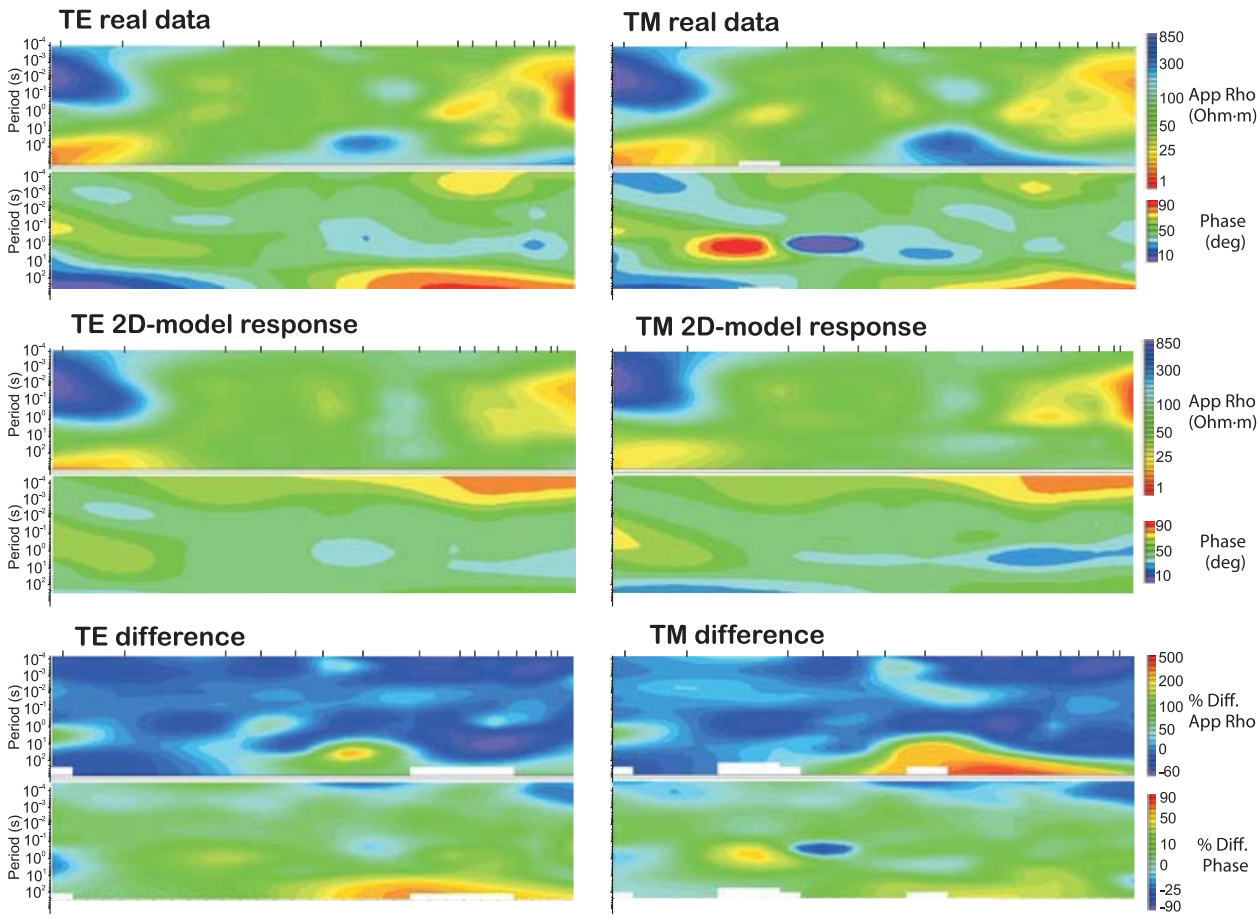

Figure 6. Magnetotelluric pseudosections. Apparent resistivity and phase pseudosections for the profile, for both the observed and modeled responses, as well as difference pseudosection between the observed and modeled responses. The difference pseudosection clarifies the spatial areas and period ranges that are well fit and poorly fit in the model.

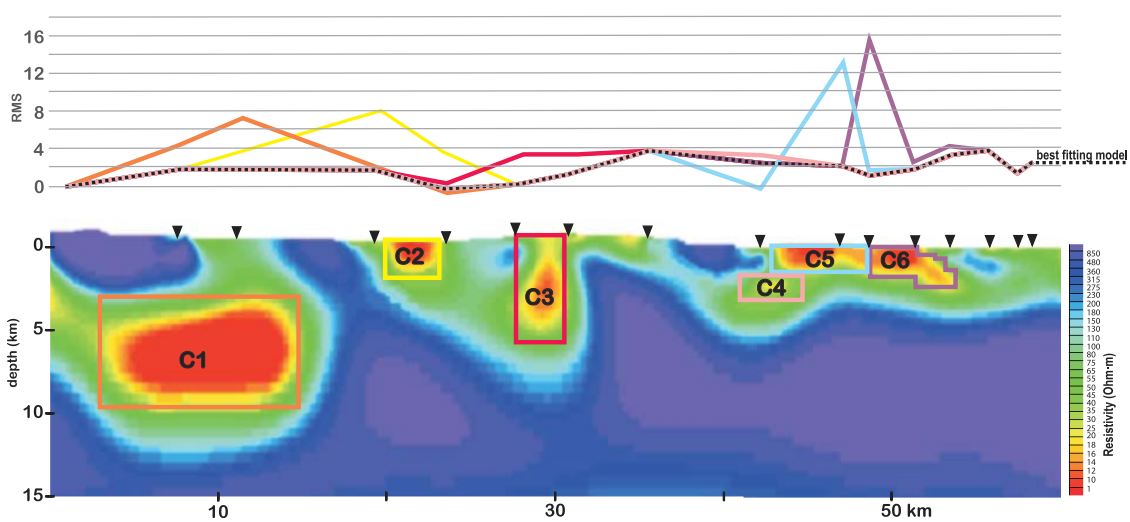

Figure 7. Sensitivity analysis. We have replaced the conductors by bodies with intermediate resistivity (100 Ω m) in the model. Each conductor returned when the inversion restarted that gives consistency to the model solution. The RMS error after replacing each conductor is marked at the top. The location of the 17 MT sites is marked.

into the ray coordinate system, using the theoretical incident angle, to obtain the respective LQT components. The L component is in the incident direction of the ray and the Q component is in the orthogonal direction to L in the vertical plane. After rotation, the P wave energy, including the direct P wave, presents in the horizontal radial component is recorded in the L component and the SV wave energy is recorded in the horizontal Q component, allowing a better observation of Ps conversions from shallow crustal discontinuities. Because in the case of a homogenous and isotropic medium the Ps conversions are recorded in the Q component, the transverse component of the P receiver function must be identically zero. Energy in the transversal component is explained by lateral heterogeneities of the isotropic medium, in particular, by dipping layers or azimuthal anisotropy. Checks on the energy of the transverse component and on its variations by back azimuth are important to provide information about the lateral variation of the media. For presentation purposes, the receiver functions were Ps moveout corrected and sorted by back azimuth in order to identify the different phases and the laterally varying structures underneath the stations (Figure 8). With the moveout correction, we try to reduce the effect of the differences in ray parameters (i.e., differences in distance) in the converted phase arrival times before stacking.

[18] The obtained P receiver functions, stacked in bins of 10° of back azimuth with an overlapping of 5°, are displayed in Figure 8a (ALHA, ASCB and ENIJ stations) and Figure 8b (ACBG and MESA stations) sorted by back azimuth. In each pair of plots, the left plots show the stacked Q components, and the right plots display the stacked T components by bins for each station. The stacking is performed after a Ps moveout correction to every receiver function using a ray parameter of 0.071 s/km as reference for the moveout. At the top left, we show the summation traces of the Q component.

[19] At stations ALHA, ENIJ and ASCB, converted phases for the Moho discontinuity are clearly observed in the Q and T component (at times T_Ps ~3.1 s, Figure 8a) as well as their multiple phases (T_Ppps ~ 10 s and T_Psps+Ppss ~13 s, Figure 8a). This allows a precise identification of this discontinuity. In the case of ACBG and MESA, the absence of a clear converted phase in a large back azimuth range (50°–240°) (T_Ps ~ 2.5 s) makes it necessary to identify the multiple converted phases (as for ACBG station, T_Ppps ~8 s and T_Psps+Ppss ~11 s) and/or identify these phases in the T component (clearer in the case of MESA), as seen in Figure 8b. The absence of the converted phase at the Moho discontinuity in these stations is apparently caused by combinations of an amplitude decrease at those back azimuths due to the Moho dip, as we will discuss later, and the interaction with Psps + Ppss multiple phases (negative amplitude) produced at a shallow discontinuity. This intracrustal discontinuity is even shallower for the northern stations (ALHA, ASCB and ENIJ) than for the southern stations (ACBG and MESA), see arrival times for the converted phase at this discontinuity in Table 2. For this reason, the interaction between their multiple and converted phases in the Moho is not clearly seen in the southern stations, where the intracrustal multiple phases arrive either later or at the same time as the Moho converted phases.

Figure 8. (a) P receiver functions for ALHA, ASCB, and ENIJ stations. In each pair of plots, the left (right) plot shows the stacked Q (T) components of the receiver function sorted by back azimuth. After performing a Ps moveout correction to every receiver function, we stack them into bins of 10° of back azimuth with an overlapping of 5°. We use a ray parameter of 0.071 s/km as reference for the moveout. At the top left, the summation trace of the Q components is displayed. The average Moho depth for these stations is ~25.1 ± 0.7 km (Table 1). The dashed red lines show arrival times for the converted phase at the Moho discontinuity (Ps) and its multiples (Ppps and Psps) for a Moho depth of 25 km, average Vp of 6.3 km/s, and Vp/vs of 1.73. The blue dashed lines mark the arrival times of converted phase in the intracrustal layer. (b) Same as Figure 8a but for ACBG and MESA stations sorted by back azimuth. The average Moho depth for these stations is ~20 ± 0.4 km (Table 1). The dashed red lines show the arrival times for the converted phase at the Moho discontinuity (Ps) and its multiples (Ppps and Psps) for a Moho depth of 20 km, average Vp of 6.3 km/s, and Vp/vs of 1.73. The blue dashed lines mark the arrival times of converted phase in the intracrustal layer. (c) Theoretical receiver function for an Earth model of one dipping layer 20 km thick over a half-space with a Vp of 6.3 km/s and a Vp/Vs of 1.73. The left pair of plots attempts to reproduce the observation for ACBG station (named ACBG_TEO) using the obtained strike 253° (N73°E) and a NNW dip of 10°. The right pair of plots is meant to reproduce the observation for MESA station (named MESA_TEO) using the obtained strike 232° (N52°E) and a NWN dip of 20°. For both stations we superimpose, with a continuous thin light gray line in the Q components, the predicted receiver function for the same model without dipping.

5.2. Moho Depths

[20] To calculate Moho depths, we use the relative traveltimes for the converted phase at the Moho discontinuity Ps, and its multiples PpPms, PpSms+PsPms phases with respect to the P arrival. These relative traveltimes can be employed to constrain the thickness (H) and Vp/Vs ratio of the crust if the average P wave velocity is known [*Zandt and Ammon*, 1995]. We apply a receiver function stacking technique developed by *Zhu and Kanamori* [2000], which enhances coherent phases and eliminates noncoherent signals if the number of records is large enough. Their methodology consists in performing a grid search over the Moho depth (H) and the

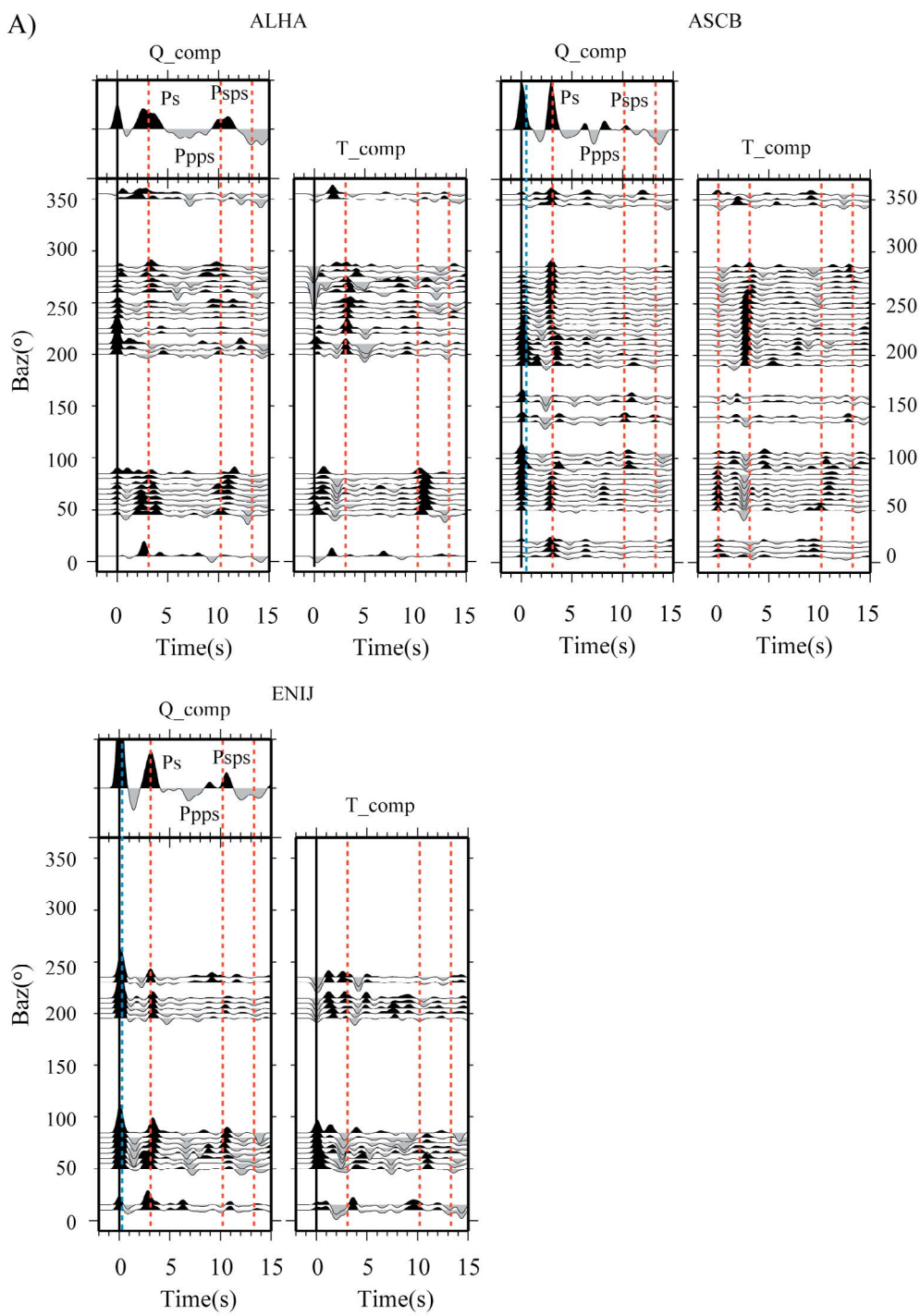

Figure 8

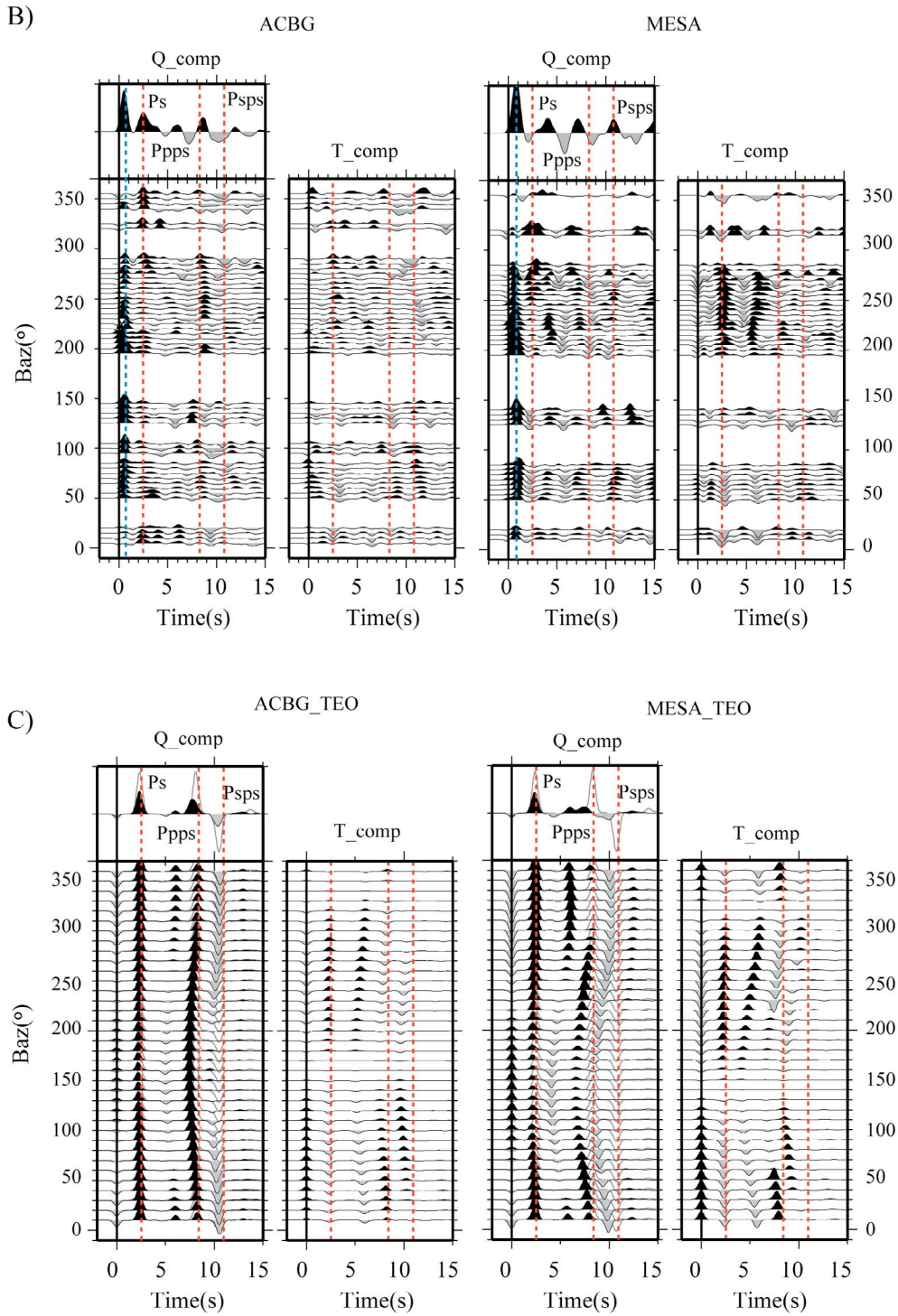

Figure 8. (continued)

average Vp/Vs in the crust, looking for the maximum of the stacking function:

$$s(H, Vp/Vs) = \sum_j \omega_1 \, RF_j(T_Ps) + \omega_2 \, RF_j(T_Ppps) - \omega_3 \, RF_j(T_Psps{+}Ppss),$$

where $RF_j(t)$ is the amplitude of the jth receiver function at time t. The summation is over all receiver functions and the ω_i are a priori phase weighting factor ($\omega_1 = 0.4$ and $\omega_2 = \omega_3 = 0.3$). The location of the maximum in the stacking surface,

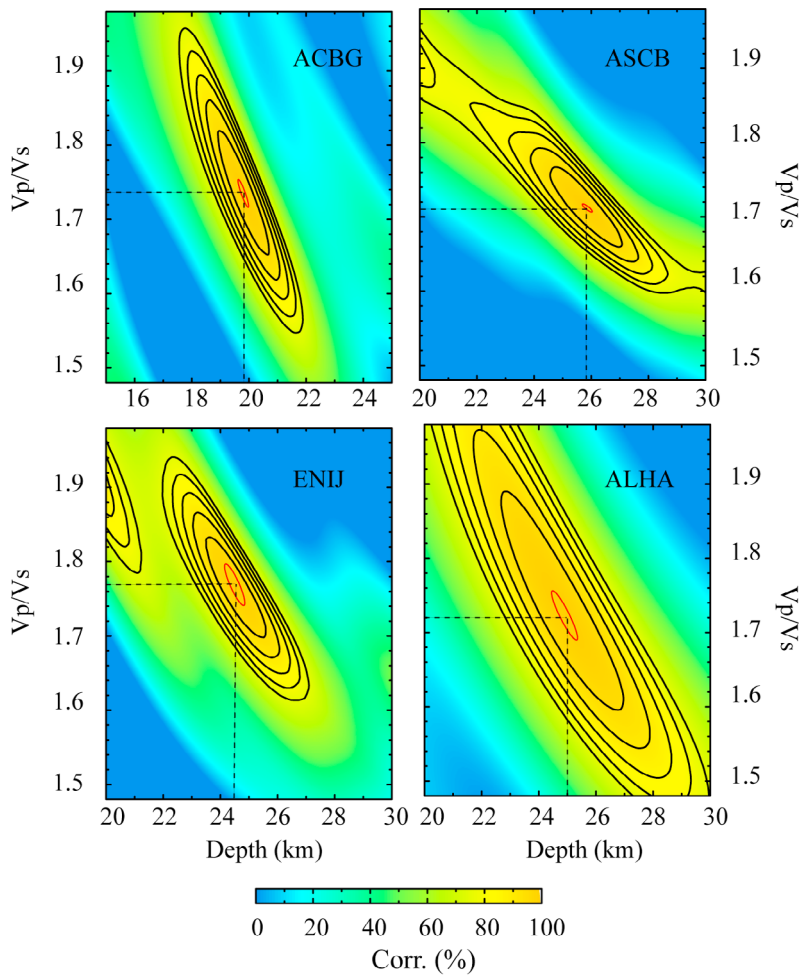

Figure 9. The grid search results to obtain the Moho depth and the Vp/Vs ratio using the Zhu and Kanamori method. The values are displayed in Table 1. The maximum of the stacking function is marked with dashed lines. The stacking surfaces (normalized to 100%) are shown along with the 1-σ confidence ellipses (red ellipse). The average Vp velocity is 6.3 km/s for the crust, after *Banda and Ansorge* [1980].

therefore, provides the estimates for H and Vp/Vs (see Figure 9). We performed this grid search in the H and Vp/Vs space using grid steps of 0.1 km and 0.01, respectively. Since the new domain is independent of ray parameters, this technique allows us to directly stack all the available records, provided that the medium is laterally homogeneous and isotropic. To estimate the uncertainties, we used a bootstrap approach [e.g., *Julià and Mejías*, 2004]. We based our statistic on 200 bootstrap replications.

[21] Some method limitations are the presence of a dipping Moho, a gradational crust-mantle boundary instead of a sharp one, or a well-defined Moho discontinuity and sedimentary environments, where the multiples from the sediment-bedrock interface overlap in time with the Ps converted phase at the Moho [e.g., *Julià et al.*, 2004]. The application of this methodology to dipping structure leads in general to an underestimation of the Moho depth and an overestimation of the Vp/Vs ratio, depending on the back azimuth coverage [*Lombardi et al.*, 2008].

[22] The obtained values for the Moho depth (H^{Zhu}) and Vp/Vs ratio (Vp/Vs^{Zhu}) using this methodology are displayed in Table 1 and the stacking surfaces (normalized to 100%) are shown in Figure 9 along with the 1−σ confidence ellipses (red) from the bootstraps analysis. The average Vp used in this grid search is 6.3 km/s in the crust, after *Banda and Ansorge* [1980].

[23] The presence of energy in the transversal component at the arrival time of the Moho converted phase and its multiples (e.g., at times T_Ps ~3.1 s, T_Ppps ~10 s and T_Psps+Ppss ~13 s for

Table 1. Moho Depths

Stations	Number of RF	Tps (s)	H^{Ps} (km)	H^{Zhu} (km)	Vp/Vs^{Zhu}	$Corr^{Zhu}$ (%)	Strike (deg)	Dip (deg)
ACBG	94	2.5	20.3	19.8 ± 0.4	1.74 ± 0.04	92	253 ± 10 (N73E)	343
ALHA	34	3.1	25.1	24.9 ± 0.9	1.72 ± 0.02	92	255 ± 21 (N75E)	345
ASCB	115	3.1	25.1	25.9 ± 0.04	1.71 ± 0.01	93	235 ± 10 (N55E)	325
ENIJ	26	3.1	25.1	24.5 ± 0.07	1.77 ± 0.06	88	245 ± 20 (N65E)	353
MESA	55	2.5	20.3				232 ± 17 (N52E)	322

ASCB station), and its amplitude variations with respect to the back azimuth (e.g., polarity change of the amplitude at back azimuth ~ 160° for ASCB station), reveals a dipping Moho beneath all the stations (Figures 8a and 8b) [*Cassidy*, 1992]. Nevertheless, the stacking procedure gets stable results for four of the stations where the converted phase and the multiples are visible in a wide range of back azimuths (Figures 8a and 8b), providing confidence in the obtained results (Figure 9 and Table 1, named H^{Zhu} and Vp/Vs^{Zhu}).

[24] For the MESA station, the above methodology is not applicable because of the lack of clear multiples and the absence of the Moho converted phase at the Q components for a wide range of back azimuths (Figure 8b). In order to get a Moho depth value for the MESA station, we calculate it simply using the arrival time of the conversion phase, without information about the multiples (Table 1, H^{Ps}). We peak the Ps arrival in the Q component summation trace of the ones with a clear conversion phase in the Q and T components after applying a Ps moveout correction. Then, we convert it to depth using a Vp/Vs of 1.73 for the whole region and an average Vp velocity of 6.3 km/s, obtained from previous refraction profiles in the area [e.g., *Banda et al.*, 1993; *Fernández et al.*, 2004]. To asses this Moho depth value for MESA station, we calculate Moho depth values for the rest of the stations using the same procedure, measuring the arrival time of the conversion phase (Table 1, H^{Ps}). Comparing the values obtained with the Zhu and Kanamori technique with the ones calculated with the arrival time of the conversion phase, we observe that both values are very similar (Table 1, H^{Zhu} and H^{Ps}) giving us confidence in the Moho depth for MESA station.

[25] In Figure 10 we present the Q component summation traces for the five stations after applying the Ps moveout correction. We sorted the traces by the arrival time of the converted phase at Moho depth. The results show that while the stations located to the north of the CFZ (ALHA, ASCB, and ENIJ) reflect a Moho located at ~25 km depth, the station located to the south of the CFZ presents a Moho at ~20 km depth (ACBG, and MESA, Figure 10).

5.3. Strike and Dip of the Moho

[26] As previously mentioned, a dipping Moho produces some effects in the Q and T components of the receiver function [*Cassidy*, 1992]. Some of these effects are the energy in the transversal component at the arrival time of the Moho converted phase and its multiples, and the variations of the amplitude in the Q and T components with back azimuth at times t = 0 and t = Tps (time of the converted phase) (including a polarity change in the T component at the downdip and updip direction, but in opposite ways) occur at times t = 0 and t = T_Ps (time of the converted phase at the intracrustal discontinuity). These changes in amplitude and polarity present a periodicity of π with back azimuth. Finally, a change in amplitude is observed at the time t = 0 and Tps in the Q and T components with back azimuth again with a π periodicity. In comparison to a flat Moho, the summation traces show a decrease in the arrival times of the converted and multiple phases with increasing dip, and the multiple phases are broader and weaker.

[27] We can recognize some of these effects in all the calculated receiver functions. The strongest

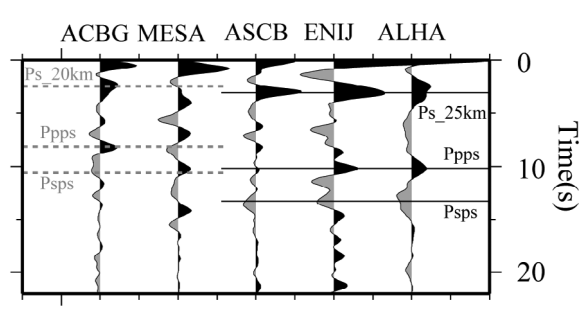

Figure 10. Receiver function Q component summation traces. We sorted the traces by the arrival time of the converted phase at Moho depth. With dashed gray lines (solid black lines), we mark the arrival times for the Moho converted phase and its multiples at 20 km depth (25 km depth).

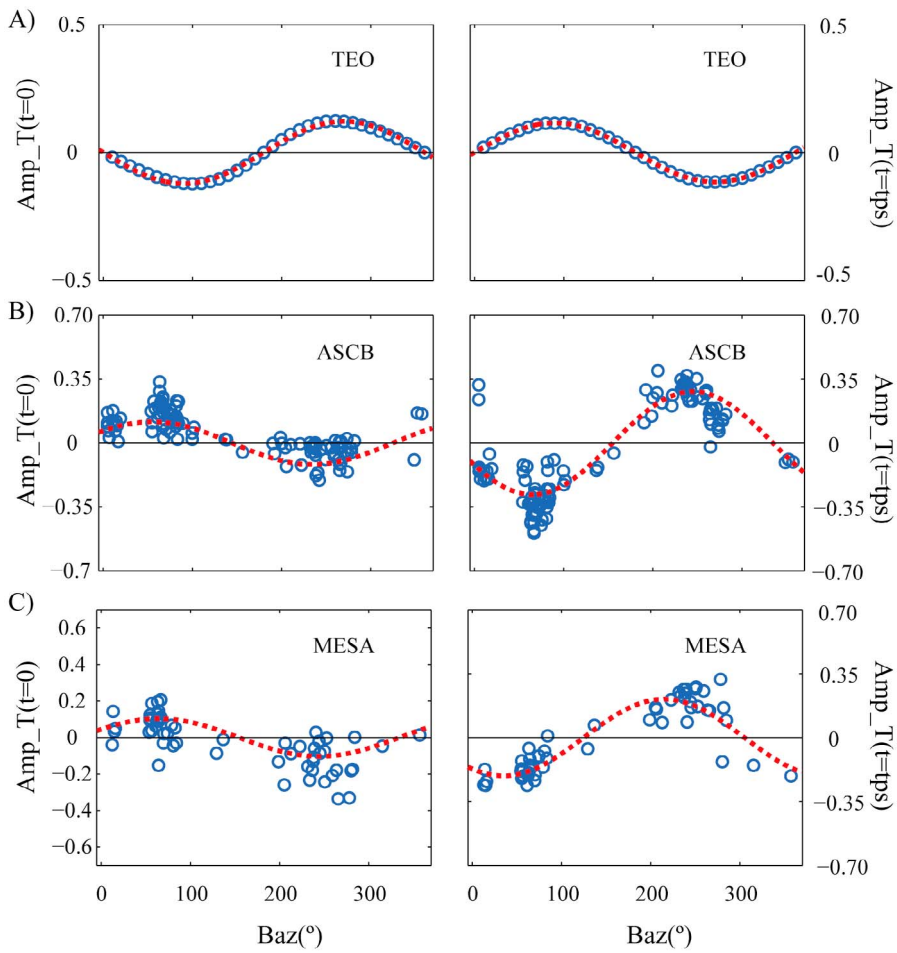

Figure 11. Fits of the periodicity with back azimuth in the amplitude variations of the T receiver function components (left) at time 0 and (right) at the arrival time of the converted phase in the Moho discontinuity (tps). Red dashed lines correspond to the fit, and the blue circles correspond to the observed amplitudes. Fit to (a) theoretical receiver function calculated for a layer of 25 km thickness over a half-space with a N90° strike direction and 180° dip direction and 15° of dipping, (b) the observed amplitudes in ASCB station, and (c) the observed amplitudes in MESA station.

effects are recorded in ASCB, ENIJ and MESA stations, where the dip and the velocity contrast of the Moho interface are greater than in ACBG and ALHA stations. The clearest features supporting the dipping of the Moho discontinuity are the presence of polarity changes at the arrival times of the converted phase in the Moho, and its multiples in the T component. These are observed for all the stations with different strength (Figure 8, left plots for each station).

[28] To obtain the Moho strike and dip direction we fit the periodicity of the amplitude variations of the T component at t = 0 and t = Tps with back azimuth. We only use the T component because the converted phase at the Moho discontinuity is not contaminated with energy of the intracrustal layers, as we can see in the Q components. We used the following expressions to calculate the fitting:

$$\mathrm{Am_T}(t = 0) = A + B\cos(\mathrm{baz} - \mathrm{strike} - 180^\circ)$$

$$\mathrm{Am_T}(t = \mathrm{tps}) = A + B\cos(\mathrm{baz} - \mathrm{strike})$$

where Am_T(t = 0) is the amplitude of the T components at the time of the direct P arrival (considered here time zero), baz is the back azimuth, and A and B are two coefficients which depend mainly on the velocity contrast and the amount of dipping. The dip direction is 90° from the obtained strike angle. Therefore, we obtain two values to calculate the strike, one from each expression (the result being the average of both, Table 1). As an example, in Figure 11 we apply the

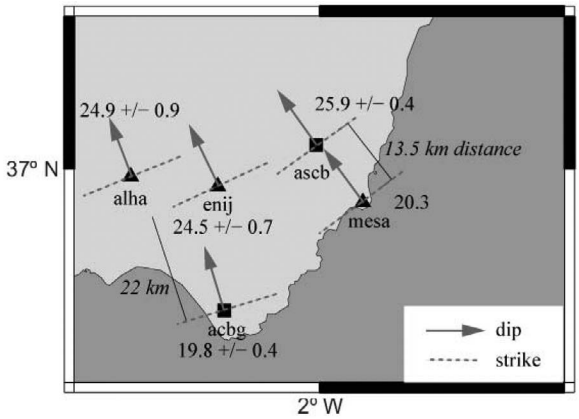

Figure 12. Map with the location of permanent (black square) and temporary (black triangle) seismic stations, showing the obtained Moho strike (dashed gray lines) and dip directions (gray arrows). Numbered close to the station locations are the obtained Moho depths. Given in italics are the distances between MESA and ACBG (~13.5 km) and between ACBG and ENIJ (~22 km) following the dip direction.

fit obtained (dashed red line) using the above expressions to theoretical amplitudes (blue circles) calculated using the Frederiksen's code [*Frederiksen and Bostock*, 2000] for one 15° south dipping layer with a strike of N90°E over a half-space (Figure 11a), the observed amplitudes (blue circles) recorded in the ASCB station (Figure 11b), and the observed amplitudes (blue circles) recorded in the MESA station (Figure 11c).

[29] Strike analysis indicates consistent ENE-WSW strike and NNW dip directions of the Moho in all the stations (Table 1 and Figure 12). Considering the Moho depth differences (~5 km) and the distances, in dip direction, between the stations, we obtain a 20° NNW dipping Moho between MESA and ASCB (~13.5 km distance) and a 10° dipping Moho between ACBG and ENIJ (~22 km distance; Figure 12). We use these results to validate the obtained strike and dip directions by calculating theoretical receiver functions for stations ACBG (Figure 8c, ACBG_TEO) and MESA (Figure 8c, MESA_TEO) using one dipping layer 20 km thick (Vp = 6.3 km/s and a Vp/Vs = 1.73) over a half-space for comparison with actual observations (Figures 8b and 8c). The theoretical receiver functions reproduce the observations related to the presence of a dipping Moho, arrival times and the polarity change in the transversal component. This modeling supports the continuity of the Moho layer without the need of a Moho step between the Northern and Southern stations.

5.4. Intracrustal Discontinuities

[30] The observation of a converted phase arriving before the converted Moho phase is clear for the stations ACBG and MESA, and less clear but present for the stations ASCB and ENIJ (blue dashed lines in Figures 8a and 8b). In view of arrival times, the conversion could come from a sediment-bedrock discontinuity or an intracrustal discontinuity. Despite the present of the Níjar-Almería sedimentary basin in the middle of study area (Figure 1), the location of the stations on rock sites (metamorphic rocks for the northern stations and volcanic rocks for the southern stations) and the absence of sediments around the stations (0.3 km around the station for 1 km sedimentary layer and Vp 4 km/s), we conclude that this converted phase corresponds to an intracrustal discontinuity. Using an average Vp of 5.6 km/s for this layer [*Banda et al.*, 1993], the depth of the discontinuity is obtained for the different stations (Table 2).

6. Discussion

[31] New magnetotelluric and seismic receiver transfer function results allow us to better characterize the subsurface structure of the eastern Betic Cordillera, deformed by the major transcurrent CFZ. Geophysical results help establish the depth and geometry of the Moho as well as intracrustal detachments that could favor shear localization controlling patterns of folding, faulting, and seismicity. In this framework, discussion of the in-depth continuity of the CFZ leads to a better understanding of strain distribution during crustal-scale transcurrent faulting.

6.1. Crustal Structure of the Upper Crust From MT and Seismic Receiver Function Correlation

[32] The geophysical data gathered here contributed to assessment of the structures in the upper crust. In particular, the MT results reveal their electrical properties interpreted in terms of lithology and fluid content variations, while receiver

Table 2. Intermediate Crustal Layer

Stations	Tps (s)	~H^{Ps} (km)
ACBG	0.5	3.8
ASCB	0.1	0.8
ENIJ	0.1	0.8
MESA	0.8	6.0

function results highlight seismic discontinuities that may be correlated with the major tectonic contacts cropping out between metamorphic complexes (Table 2).

[33] The southern part of the MT resistivity inversion model (Figure 5) features the conductors C5 and C6, which extend down to approximately 1.5 km and are associated with the outcropping sedimentary rocks of the Almería-Níjar Basin and with part of the basement metamorphic rocks, most likely water saturated. Noteworthy is the absence of a deep conductive zone associated with the CFZ, and so only the shallow conductor C6 could be associated with the uppermost part of the fault zone, where the fault gouge involves conductive sedimentary rocks including marls and gypsum. The high-resistivity feature around station 6 is probably associated with Alpujárride marbles that are unconformably covered by Upper Tortonian calcarenites and reefal systems. Eastward, the high-conductivity body C5 coincides with the marls that crops out to basinward and the increase in conductivity between stations 7 and 8 correlates with the transition between calcarenites/reefal systems and marls. In the central part of the model, the N-verging geometry of the Sierra Alhamilla antiform is seen to be surrounded by a conductive zone that reveals the geometry of the kilometric amplitude fold. This conductive zone would be associated with the Alpujárride/Nevado-Filábride contact, a folded major detachment cropping out in the Sierra Alhamilla and in the Sierra de Los Filabres antiform cores. Associated with the Alpujárride/Nevado-Filábride contact are 100 m thick mylonites and breccias, sometimes iron enriched, facilitating fluid circulation [*Galindo-Zaldívar et al.*, 1989]. The Nevado-Filábride/Alpujárride conductive zone extends beneath the Tabernas and Níjar Basins northward as well as southward of the CFZ, and can also be correlated with intracrustal seismic discontinuities detected beneath station ENIJ at 0.8 km depth, and beneath ACBG at 3.8 km depth. The intracrustal discontinuity identified at 6 km depth beneath the MESA station, placed over volcanic rocks, is interpreted as the contact between graphitic schist and schist and marbles. This contact crops out northward in the southern limb of Sierra Alhamilla and partially corresponds with a boundary between intermediate and high-resistivity sectors in the MT model. Beneath the ASCB station and placed over graphitic schist of the Nevado-Filábride complex, an intracrustal discontinuity is detected at 0.8 km depth that could either correspond to an intra-Nevado-Filábride low-angle normal fault or a contact between graphite schist and quartzites, typical of the lower part of the Nevado-Filabride complex. Northward, conductor C2 is associated with part of the sedimentary rocks that infill the Tabernas basin. Their location is restricted to the central part of the basin, coinciding with the trace of some steeply dipping normal faults associated with hot water and metallic mineralization [*Sanz de Galdeano et al.*, 2008]. A large conductive body placed beneath Sierra de Los Filabres antiform, between 4 and 9 km, corresponds with basic rocks that played a major role during the antiform nucleation [*Pedrera et al.*, 2009]. Therefore, the bottom of these basic rocks is interpreted as a crustal decoupling that allows the development of the kilometric amplitude Sierra de Los Filabres antiform in its hanging wall (Figure 13).

6.2. Deformation Style of Crustal-Scale Transcurrent Faults in Weak Decoupled Crusts

[34] After characterizing several anisotropies that could act as a detachment level in the crust of the eastern Betic Cordillera, the foremost open question is if the CFZ roots into one of these crustal detachments or if it is a crustal penetrating fault. Converted phases of the receiver function reveal that Moho depths reach ~25 km beneath the stations located northward of the CFZ and ~20 km below the stations located to the south, over the Miocene volcanic rocks of Cabo de Gata (Table 1). Some effects in the Q and T components of the receiver functions reveal the presence of a dipping Moho with a 10–20° dip to the NNW near the CFZ, confirmed by theoretical modeling of the Q and T components of the receiver functions. Furthermore, if we reconstruct the Moho topography, taking into account the 34 km depth of the refraction Moho obtained beneath Sierra de Los Filabres from the deep seismic refraction profiles [*Banda et al.*, 1993] and the regional Bouguer anomaly trend [*IGN*, 1975], the crustal thickness constantly increases, with 10–20° dipping to the NNW showing a small Moho flexure that coincides with the CFZ (Figure 13). The obtained ENE-WSW direction of the Moho is parallel to the folds and slightly oblique to the NE-SW oriented CFZ. Therefore, the increase in crustal thickness is probably connected with fold development. We do not relate the regional variation of the Moho depth to an offset associated with the CFZ activity confirmed by seismic receiver function analysis. However, a small but evident flexure at Moho coincides with the CFZ, as deduced from the Bouguer anomaly

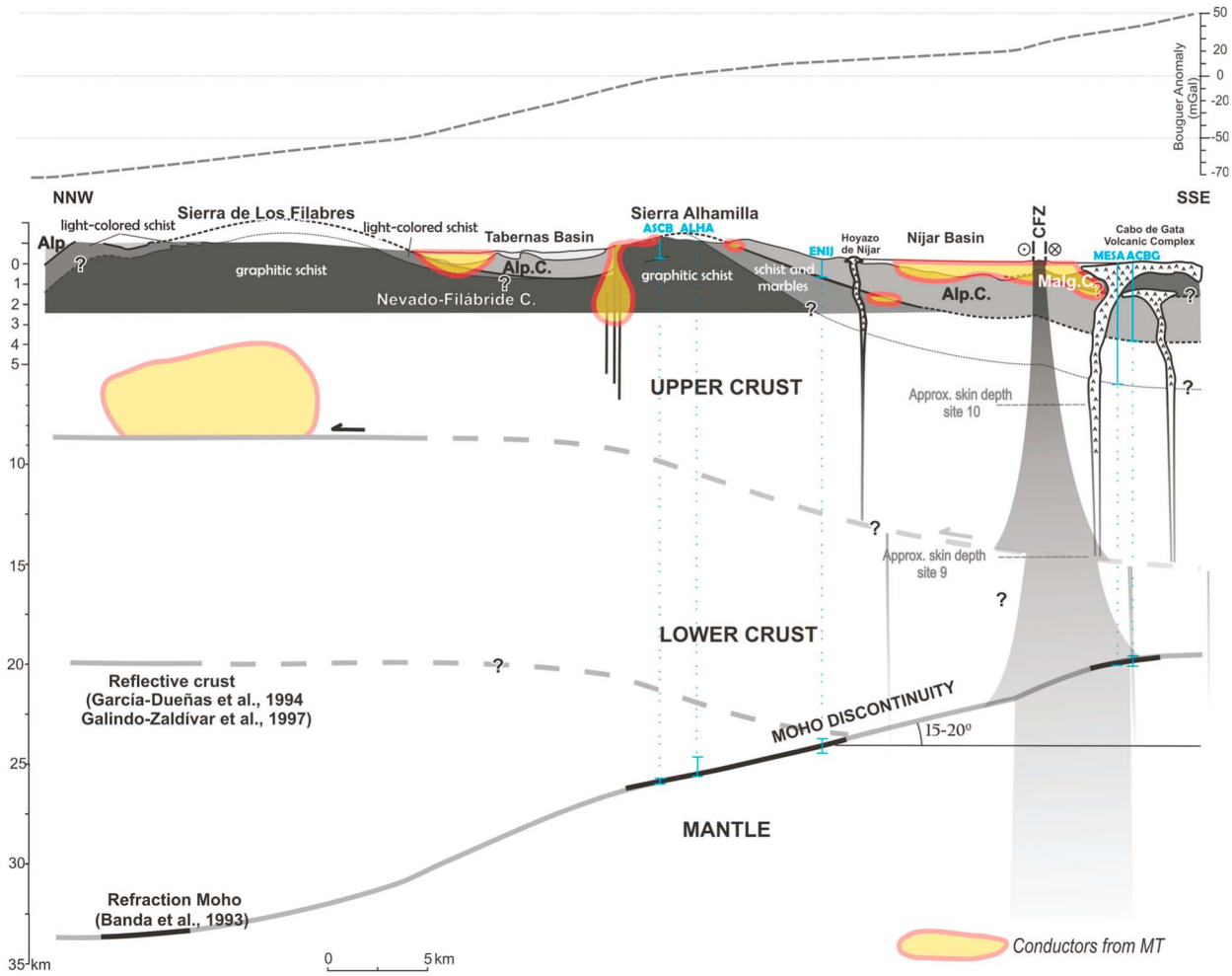

Figure 13. Crustal-scale section across the eastern Betic Cordillera that combines geological, magnetotelluric, seismic receiver function, and Bouguer anomaly data.

trend (Figure 13). The presence of a Moho flexure could involve the deformation of the CFZ reaching down to the mantle. Therefore, although the CFZ is only detected as a conductor in the uppermost part of the MT model, the obtained Bahr strike and tipper angle in the station closest to the CFZ clearly reveals the continuity of the fault zone at least down to some 15 km (Figure 4c). In addition, features such as the presence of several subparallel fault planes and the positive relief associated with the CFZ are predicted by the thermomechanical numerical models of strike-slip faulting that deform weak layered crusts [*Sobolev et al.*, 2005].

[35] A decoupling assumed approximately at 9 km at the bottom of the conductive body beneath the Sierra de Los Filabres antiform would be responsible for fold development in the upper crust. Above this detachment zone, crustal discontinuities such as the contacts between metamorphic complexes are folded, as indicated by the correlation between the field data, the MT model, and the intracrustal seismic discontinuities (Figure 13). We infer that the CFZ deforms a decoupled weak crust and partially transfers deformation across the intracrustal discontinuities. The role of low-angle discontinuities in the downdip segmentation of strike-slip fault zones has been recently studied at the outcrop scale in a southern sector of the San Jacinto fault zone in southern California [*Nemser and Cowan*, 2009], where bedding-parallel slip is detected as an important mechanism for accommodating slip within strike-slip fault zones that cut across subhorizontal heterogeneous stratigraphy.

[36] Strain numerical modeling [*Sobolev et al.*, 2005] suggests that the nucleation of large transcurrent faults is controlled by a minimum of the litho-

spheric strength associated with highest temperature of the uppermost mantle. In the eastern Betic Cordillera, the close relationship between the location of the upper Miocene volcanic rocks and the trace of strike-slip faults agrees with the prediction of strike-slip fault nucleation in regions having the highest temperature at the base of the lithosphere. Therefore, the CFZ nucleation occurs in a sector of minimum crustal thickness where melting processes critically reduced the lithospheric strength during the late Miocene. Thermal modeling results suggest present-day partial melting in the deepest crust of the eastern Betic Cordillera [*Soto et al.*, 2008]. We propose that the CFZ was probably nucleated at the base of a hot crust during the late Miocene and then propagated upward, partially transferring deformation through the subhorizontal crustal discontinuities before reaching the topographic surface. Northward, since the Late Miocene, the lithosphere is moderately stronger and the crustal discontinuities favor the development of kilometric amplitude folds instead of strike-slip faults.

6.3. Downward Extent of Transcurrent Faults and Associated Deformation

[37] The lack of a Moho offset associated with the Carboneras Fault is of particular interest in view of current debates about the nature and extent of major strike-slip faults in the lower crust and upper mantle. The results derived from seismic exploration are sometimes contradictory and the mechanisms that accommodate deformation of major transcurrent faults at depth are uncertain. Traditionally, major strike-slip fault zones that cross the whole crust are visualized as a narrow band that extends across the lower crust producing a Moho offset [*Sibson*, 1977; *Stern and McBride*, 1998]. The crustal structure across the San Andreas Fault in southern California characterized by using the common conversion point stacking of teleseismic P-to-S converted waves suggest that the deformation in the lower crust is localized and coincides with the faults segments observed in surface [*Zhu*, 2002].

[38] However, field and seismic evidences suggest that deformation along some transcurrent faults widen at depth linked to a broadening subvertical shear zone [*Lemiszki and Brown*, 1988; *Scholz*, 1988; *Chester*, 1995]. The Miocene Salzachtal-Ennstal-Mariazell-Puchberg strike-slip fault in the Austrian Alps is exposed showing the total transition from brittle to a dominantly ductile structure. The brittle fault segments westward transform to a progressively more broaden and ductile high-strain zone that are characterized by plastic mylonitic deformation corresponding with lower crustal levels [*Cole et al.*, 2007]. A passive seismic experiment characterized the deep crustal deformation of the Marlborough fault system that is associated with the boundary between the Pacific and Australian plates [*Wilson et al.*, 2004]. Teleseismic converted waves showed a nearly 10 km variation in crustal thickness from north to south beneath a fault segment that was connected by a Moho ramp. Azimuthal variations in the amplitude of the converted phases supported the dipping Moho along the ramp as well as the presence of crustal anisotropy at midcrustal levels. These observations indicate that strike-slip deformation becomes distributed over a broad region in the lower crust and upper mantle and does not produce a sharp offset of the Moho beneath the outcropping fault trace. Although the Marlborough Fault probably has about an order of magnitude larger displacement than the Carboneras Fault, our results also support the idea that some large strike-slip faults tend to accommodate the deformation by a broadening fault zone at lower crustal levels rather than extending into mantle as vertical faults with associated offset of the Moho.

7. Conclusions

[39] A new crustal-scale section across the eastern Betic Cordillera is proposed combining geological, magnetotelluric and seismic receiver functions data suggesting the development of crustal-scale transcurrent fault in a decoupled crust.

[40] Receiver P functions obtained from the records of five seismic broadband stations yielded Moho depth variations in the area near the Carboneras transcurrent fault zone and average values of the Vp/Vs ratio. The stations located northward of the major Carboneras transcurrent fault zone present a ~25 km Moho depth, while the stations located to the south show ~20 km depth, in agreement with the gradient of the Bouguer gravity anomaly. The crust gets progressively thicker toward the NNW, with 10–20° Moho dips.

[41] Kilometric amplitude folds control the central and northern part of the reconstructed section, coinciding with the sector of greater crustal thickening. In the central part of the MT model, the N-verging geometry of the Sierra Alhamilla antiform is surrounded by a conductive zone that sug-

gests the kilometric fold geometry. This conductive zone would be associated with the Alpujárride/Nevado-Filábride contact, a major folded detachment cropping out in the Sierra Alhamilla and in the Sierra de Los Filabres antiforms, which is observed as a seismic crustal discontinuity toward the south. In addition, a decoupling is inferred approximately at 9 km, at the bottom of the conductive body beneath Sierra de Los Filabres antiform regarded as responsible for the large folds in the upper crust. The calculated ENE-WSW direction of the Moho is consistently parallel to these folds, which, since the late Miocene, favored the progressive crustal thickening of a previously thin continental crust.

[42] A small flexure at Moho coinciding with the CFZ is deduced from the Bouguer anomaly trend, also agreeing with the receiver function results (Figure 13). The presence of a Moho flexure could imply that the CFZ deformation reaches down to the mantle. Therefore, the obtained Bahr strike and tipper phase in the stations placed closest to the CFZ reveal the continuity of the CFZ at least up to approximately 15 km (10 s), crossing all the detected crustal discontinuities and probably reaching up to the Moho, affecting a wide area with a more ductile deformation behavior.

[43] The lack of a clearly Moho offset associated with the Carboneras Fault is of particular interest in view of current debates about the nature and extent of major strike-slip faults in the lower crust and upper mantle, supporting the idea that some large strike-slip faults tend to accommodate the deformation by a broadening fault zone at lower crustal levels rather than extending into mantle as vertical faults with associated offset of the Moho.

[44] The CFZ nucleation could have occurred at the base of a thin crust, where melting processes critically reduced lithospheric strength during the late Miocene, to then propagate vertically upward, partially transferring deformation across the subhorizontal crustal discontinuities and reaching the topographic surface. Northward, where the lithosphere was moderately stronger, the crustal discontinuities favored the development of kilometric amplitude folds instead of strike-slip faults.

[45] The proposed model of crustal-scale transcurrent fault development explains the close relationship between the location of the late Miocene volcanic rocks and the trace of strike-slip faults in the eastern Betic Cordillera and the Alboran Sea. In addition, our study confirms the thermomechanical modeling prediction of crustal-scale transcurrent fault nucleation in regions with minimal lithospheric strength associated with thin crusts and a higher temperature of the uppermost mantle.

Acknowledgments

[46] We thank the Instituto Andaluz de Geofísica (IAG), who provided the seismic data. We acknowledge work with the free software SAC [*Goldstein et al.*, 2003] and GMT [*Wessel and Smith*, 1998]. We are very grateful to John Platt; one anonymous reviewer; and James Tyburczy, Editor of G-Cubed, for the detailed and constructive comments concerning the paper. This study was supported by projects TOPO-IBERIA CONSOLIDER-INGENIO CSD2006-00041, CGL2008-01830, P09-RNM-5100, CGL 2009 07721, and CGL 2008 0367 E/BTE of the Spanish Ministry of Science and Education, as well as by Research Groups RNM-148 and RNM-104 of the Junta de Andalucía Regional Government. Jean Sanders revised the English of the manuscript.

References

Aldaya, F., J. Campos, V. García-Dueñas, F. González-Lodeiro, and M. Orozco (1984), El contacto Alpujárrides/Nevado-Filábrides en la vertiente meridional de Sierra Nevada. Implicaciones tectónicas, in *El borde mediterráneo español: Evolución del orógeno bético y geodinámica de las depresiones neógenas*, pp. 18–20, Dep. de Invest. Geol., Cons. Super. de Invest. Cient., Granada, Spain.

Balanyá, J. C., and V. García-Dueñas (1987), Les directions structurales dans le Domaine d'Alborán de part et d'autre du Détroit de Gibraltar, *C. R. Acad. Sci., Ser. II*, *304*, 929–932.

Banda, E., and J. Ansorge (1980), Crustal structure under the central and eastern part of the Betic Cordillera, *Geophys. J. R. Astron. Soc.*, *63*, 515–532.

Banda, E., J. Gallart, V. García-Dueñas, J. J. Dañobeitia, and J. Makris (1993), Lateral variation of the crust in the Iberian Peninsula: New evidence from the Betic Cordillera, *Tectonophysics*, *221*, 53–66, doi:10.1016/0040-1951(93)90027-H.

Bertrand, E., M. Unsworth, C. W. Chiang, C. S. Chen, C. C. Chen, F. Wu, E. Türkoğlu, H.-L. Hsu, and G. Hill (2009), Magnetotelluric evidence for thick-skinned tectonics in central Taiwan, *Geology*, *37*, 711–714, doi:10.1130/G25755A.1.

Blumenthal, M. (1927), Versuch einer tektonischen Gliederung der Betischen Kordilleren von Central und Sùdwest Andalusien, *Eclogae Geol. Helv.*, *20*, 487–592.

Booth-Rea, G., C. R. Ranero, J. M. Martínez-Martínez, and I. Grevemeyer (2007), Crustal types and Tertiary tectonic evolution of the Alborán sea, western Mediterranean, *Geochem. Geophys. Geosyst.*, *8*, Q10005, doi:10.1029/2007GC001639.

Bousquet, J. C., and C. Montenat (1974), Présence de décrochement Nord-Est, Sud-Ouest plioquaternaires dans les Cordillères bétiques orientales (Espagne). Extension et signification générale, *C. R. Seances Acad. Sci., Ser. C*, *278*, 2617–2620.

Butler, R., and S. Mazzoli (2006), Styles of continental contraction: A review and introduction, *Spec. Pap. Geol. Soc. Am.*, *414*, 1–10, doi:10.1130/2006.2414(01).

Caldwell, T. G., H. M. Bibby, and C. Brown (2004), The magnetotelluric phase tensor, *Geophys. J. Int.*, *158*, 457–469, doi:10.1111/j.1365-246X.2004.02281.x.

Cassidy, J. F. (1992), Numerical experiments in broad-band receiver function—Analysis, *Bull. Seismol. Soc. Am.*, *82*, 1453–1474.

Chester, F. M. (1995), A rheologic model for wet crust applied to strike-slip faults, *J. Geophys. Res.*, *100*, 13,033–13,044, doi:10.1029/95JB00313.

Cole, J., B. Hacker, L. Ratschbacher, J. Dolan, G. Seward, E. Frost, and W. Frank (2007), Localized ductile shear below the seismogenic zone: Structural analysis of an exhumed strike-slip fault, Austrian Alps, *J. Geophys. Res.*, *112*, B12304, doi:10.1029/2007JB004975.

Crespo-Blanc, A., and J. Campos (2001), Structure and kinematics of the South Iberian paleomargin and its relationship with the Flysch Trough units: Extensional tectonics within the Gibraltar Arc fold-and- thrust belt (western Betics), *J. Struct. Geol.*, *23*, 1615–1630, doi:10.1016/S0191-8141(01)00012-8.

De Larouzière, F. D., J. Bolze, P. Bordet, J. Hernández, C. Montenat, and P. Ott d'Estevou (1988), The Betic segment of the lithospheric Trans-Alboran shear zone during the Late Miocene, *Tectonophysics*, *152*, 41–52, doi:10.1016/0040-1951(88)90028-5.

Dewey, J. F., M. L. Helman, E. Turco, D. H. W. Hutton, and S. D. Knott (1989), Kinematics of the western Mediterranean, in *Alpine Tectonics*, edited by M. P. Coward, D. Dietrich, and R. G. Park, *Geol. Soc. Spec. Publ.*, *45*, 265–283.

Doll, W. E., W. J. Domoracki, J. K. Costain, C. Çoruh, A. Ludman, and J. T. Hopeck (1996), Seismic reflection evidence for the evolution of a transcurrent fault system: The Norumbega fault zone, Maine, *Geology*, *24*, 251–254, doi:10.1130/0091-7613(1996)024<0251:SREFTE>2.3.CO;2.

Duggen, S., K. Hoernle, A. Kluegel, J. Geldmacher, M. Thirlwall, F. Hauff, D. Lowry, and N. Oates (2008), Geochemical zonation of the Miocene Alboran Basin volcanism (westernmost Mediterranean): Geodynamic implications, *Contrib. Mineral. Petrol.*, *156*, 577–593, doi:10.1007/s00410-008-0302-4.

Egeler, C. G. (1963), On the tectonics of the eastern Betic Cordilleras (SE Spain), *Geol. Rundsch.*, *52*, 260–269.

Fadil, A., P. Vernant, S. McClusky, R. Reilinger, F. Gomez, D. B. Sari, T. Mourabit, K. Feigl, and M. Barazangi (2006), Active tectonics of the western Mediterranean: Geodetic evidence for rollback of a delaminated subcontinental lithospheric slab beneath the Rif Mountains, Morocco, *Geology*, *34*, 529–532, doi:10.1130/G22291.1.

Faulkner, D. R., A. C. Lewis, and E. H. Rutter (2003), On the internal structure and mechanics of large strike-slip fault zones: Field observations of the Carboneras fault in southeastern Spain, *Tectonophysics*, *367*, 235–251, doi:10.1016/S0040-1951(03)00134-3.

Faulkner, D. R., T. M. Mitchell, E. H. Rutter, and J. Cembrano (2008), On the structure and mechanical properties of large strike-slip faults, *Geol. Soc. Spec. Publ.*, *299*, 139–150, doi:10.1144/SP299.9.

Fernández, M., I. Marzan, and M. Torné (2004), Lithospheric transition from the Variscan Iberian Massif to the Jurassic oceanic crust of the central Atlantic, *Tectonophysics*, *386*, 97–115, doi:10.1016/j.tecto.2004.05.005.

Frederiksen, A. W., and M. G. Bostock (2000), Modelling teleseismic waves in dipping anisotropic structures, *Geophys. J. Int.*, *141*, 401–412, doi:10.1046/j.1365-246x.2000.00090.x.

Galindo-Zaldívar, J., F. González Lodeiro, and A. Jabaloy (1989), Progressive extensional shear structures in a detachment contact in the western Sierra Nevada (Betic Cordilleras, Spain), *Geodin. Acta*, *3*, 73–85.

Galindo-Zaldívar, J., A. Jabaloy, F. González-Lodeiro, and F. Aldaya (1997), Crustal structure of the central sector of the Betic Cordillera (SE Spain), *Tectonics*, *16*, 18–37, doi:10.1029/96TC02359.

García-Dueñas, V., J. M. Martínez-Martínez, M. Orozco, and J. Soto (1988), Plisnappes, cisillements syn- à post-métamorphiques et cisaillements ductiles fragiles en distension dans les Nevado-Filabrides (Cordillères bétiques, Espagne), *C. R. Acad. Sci., Ser. II*, *307*, 1389–1395.

García-Dueñas, V., E. Banda, M. Torné, D. Córdoba, and the ESCI-Béticas Working Group (1994), A deep seismic reflection survey across the Betic Chain (southern Spain): First results, *Tectonophysics*, *232*, 77–89, doi:10.1016/0040-1951(94)90077-9.

Goldstein, P., D. Dodge, M. Firpo, and L. Minner (2003), SAC2000: Signal processing and analysis tools for seismologists and engineers, in *International Handbook of Earthquake and Engineering Seismology, Part B*, pp. 1613–1614, Academic, Amsterdam.

Gràcia, E., et al. (2006), Active faulting offshore SE Spain (Alboran Sea): Implications for earthquake hazard assessment in the Southern Iberian Margin, *Earth Planet. Sci. Lett.*, *241*, 734–749, doi:10.1016/j.epsl.2005.11.009.

Hanmer, S. (1988), Great Slave Lake Shear Zone: Reconstructed vertical profile of a crustal scale fault zone, *Tectonophysics*, *149*, 245–264, doi:10.1016/0040-1951(88)90176-X.

Hole, J. A., B. C. Beaudoin, and S. L. Klemperer (2000), Vertical extent of the newborn San Andreas fault at the Mendocino triple junction, *Geology*, *28*(12), 1111–1114, doi:10.1130/0091-7613(2000)28<1111:VEOTNS>2.0.CO;2.

Instituto Geográfico Nacional (IGN) (1975), Mapa de España de Anomalía de Bouguer, scale 1:1,000,000, Madrid.

Julià, J., and J. Mejías (2004), Thickness and v_p/v_s ration variation n the Iberian crust, *Geophys. J. Int.*, *156*, 59–72, doi:10.1111/j.1365-246X.2004.02127.x.

Julià, J., C. J. Ammon, and R. B. Herrmann (2004), Evaluation of deep sediment velocity structure in the New Madrid seismic zone, *Bull. Seismol. Soc. Am.*, *94*, 334–340, doi:10.1785/0120030081.

Keller, J. V. A., S. H. Hall, C. J. Dart, and K. R. Mc Clay (1995), The geometry and evolution of a transpressional strike-slip system: The Carboneras fault, SE Spain, *J. Geol. Soc.*, *152*, 339–351, doi:10.1144/gsjgs.152.2.0339.

Langston, C. A. (1979), Structure under Mount Rainier, Washington, inferred from telesismic body waves, *J. Geophys. Res.*, *84*, 4749–4762, doi:10.1029/JB084iB09p04749.

Lemiszki, P. J., and L. D. Brown (1988), Variable structure of strike-slip fault zones as observed on deep seismic reflection profiles, *Geol. Soc. Am. Bull.*, *100*, 665–676, doi:10.1130/0016-7606(1988)100<0665:VCSOSS>2.3.CO;2.

Ligorria, J. P., and C. J. Ammon (1999), Iterative deconvolution and receiver function estimation, *Bull. Seismol. Soc. Am.*, *89*, 1395–1400.

Lombardi, D., J. Braunmiller, E. Kissling, and D. Giardini (2008), Moho depth and Poisson's ratio in the western-central Alps from receiver functions, *Geophys. J. Int.*, *173*, 249–264, doi:10.1111/j.1365-246X.2007.03706.x.

Lonergan, L., and N. White (1997), Origin of the Betic-Rif Mountain belt, *Tectonics*, *16*, 504–522, doi:10.1029/96TC03937.

Luján, M., F. Storti, J. C. Balanyá, A. Crespo-Blanc, and F. Rossetti (2003), Role of decollement material with different rheological properties in the structure of the Aljibe thrust imbricate (Flysch Trough, Gibraltar Arc): An analogue modelling approach, *J. Struct. Geol.*, *25*, 867–881, doi:10.1016/S0191-8141(02)00087-1.

Mackie, R., J. Smith, and T. R. Madden (1994), Three-dimensional modeling using finite difference equations: The magnetotelluric example, *Radio Sci.*, *29*, 923–935, doi:10.1029/94RS00326.

Martí, A., P. Queralt, E. Roca, J. Ledo, and J. Galindo-Zaldivar (2009), Geodynamic implications for the formation of the Betic-Rif orogen from magnetotelluric studies, *J. Geophys. Res.*, *114*, B01103, doi:10.1029/2007JB005564.

Martínez-Martínez, J. M., and J. M. Azañón (1997), Mode of extensional tectonics in the southeastern Betics (SE Spain): Implications for the tectonic evolution of the peri-Alborán orogenic system, *Tectonics*, *16*, 205–225, doi:10.1029/97TC00157.

Mazzoli, S., and M. L. Helman (1994), Neogene patterns of relative plate motion for Africa-Europe: Some implications for recent central Mediterranean tectonics, *Geol. Rundsch.*, *83*, 464–468.

Montenat, C., and P. Ott d'Estevou (1990), Eastern Betic Neogene basins—A review, in *Les Bassins Neogenes du Domaine Betique Orientale (Espagne)*, *Doc. et Travaux de l'Inst. Geol. Albert de Lapparent*, vol. 12–13, edited by C. Montenat, pp. 9–15, Inst. Geol. Albert de Lapparent, Paris.

Moreno, X., E. Masana, E. Gràcia, R. Pallàs, P. Ruano, M. Coll, P. Tepancíková, and P. Santanach (2007), First evidence of paleoearthquakes in Carboneras Fault: A Paleoseismological study in La Serrata, *Geogaceta*, *41*, 135–138.

Müller, P. D., and W. R. Roest (1992), Fracture zones in the North Atlantic from combined Geosat and Seasat data, *J. Geophys. Res.*, *97*, 3337–3350, doi:10.1029/91JB02605.

Nemser, E. S., and D. S. Cowan (2009), Downdip segmentation of strike-slip fault zones in the brittle crust, *Geology*, *37*, 419–422.

Ott d'Estevou, P., and C. Montenat (1985), Évolution structurale de la zone bétique orientale (Espagne) du Tortonien à l'Holocène, *C. R. Acad. Sci., Ser. II*, *300*, 363–368.

Pedrera, A., C. Marín-Lechado, J. Galindo-Zaldívar, L. R. Rodríguez-Fernández, and A. Ruiz-Constán (2006), Fault and fold interaction during the development of the Neogene-Quaternary Almería-Níjar basin (SE Betic Cordilleras), in *Tectonics of the Western Mediterranean and North Africa*, edited by G. Moratti and A. Chalouan, *Geol. Soc. Spec. Publ.*, *262*, 217–230.

Pedrera, A., J. Galindo-Zaldívar, A. Ruíz-Constan, C. Duque, C. Marín-Lechado, and I. Serrano (2009), Recent large fold nucleation in the upper crust: Insight from gravity, magnetic, magnetotelluric and seismicity data (Sierra de Los Filabres-Sierra de Las Estancias, Internal Zones, Betic Cordillera), *Tectonophysics*, *463*, 145–160, doi:10.1016/j.tecto.2008.09.037.

Platt, J. P., and R. L. M. Vissers (1989), Extensional collapse of thickened continental lithosphere: A working hypothesis for the Alboran Sea and Gibraltar arc, *Geology*, *17*, 540–543, doi:10.1130/0091-7613(1989)017<0540:ECOTCL>2.3.CO;2.

Pous, J., P. Queralt, J. Ledo, and E. Roca (1999), A high electrical conductive zone at lower crustal depth beneath the Betic Chain (Spain), *Earth Planet. Sci. Lett.*, *167*, 35–45, doi:10.1016/S0012-821X(99)00011-4.

Rodi, W., and R. L. Mackie (2001), Nonlinear conjugate gradients algorithm for 2-D magnetotelluric inversion, *Geophysics*, *66*, 174–187, doi:10.1190/1.1444893.

Rosenbaum, G., G. S. Lister, and C. Duboz (2002), Relative motions of Africa, Iberia and Europe during Alpine orogeny, *Tectonophysics*, *359*, 117–129, doi:10.1016/S0040-1951(02)00442-0.

Roy, M., and L. H. Royden (2000), Crustal rheology and faulting at strike-slip plate boundaries: 2. Effects of lower crustal flow, *J. Geophys. Res.*, *105*, 5599–5613, doi:10.1029/1999JB900340.

Royden, L. H. (1993), Evolution of retreating subduction boundaries formed during continental collision, *Tectonics*, *12*, 629–638, doi:10.1029/92TC02641.

Rutter, E. H., R. H. Maddock, S. H. Hall, and S. H. White (1986), Comparative microstructures of natural and experimentally produced clay-bearing fault gouges, *Pure Appl. Geophys.*, *124*, 3–30, doi:10.1007/BF00875717.

Sanz de Galdeano, C., J. Galindo-Zaldívar, S. Morales, M. López-Chicano, J. M. Azañón, and W. Martín Rosales (2008), Travertines linked to faults. Examples from the Tabernas desert (Almería, Betic Cordillera), *Geogaceta*, *45*, 31–35.

Scholz, C. H. (1988), The brittle-plastic transition and the depth of seismic faulting, *Geol. Rundsch.*, *77*, 319–328, doi:10.1007/BF01848693.

Scotney, P., R. Burgess, and E. H. Rutter (2000), $^{40}Ar/^{39}Ar$ age of the Cabo the Gata volcanic series and displacements on the Carboneras fault zone, SE Spain, *J. Geol. Soc.*, *157*, 1003–1008, doi:10.1144/jgs.157.5.1003.

Sibson, R. H. (1977), Fault rocks and fault mechanisms, *J. Geol. Soc.*, *133*, 191–213, doi:10.1144/gsjgs.133.3.0191.

Simpson, F., and K. Bahr (2005), *Practical Magnetotellurics*, 270 pp., doi:10.1017/CBO9780511614095, Cambridge Univ. Press, Cambridge, U. K.

Sobolev, S. V., A. Petrunin, Z. Garfunkel, and A. Y. Babeyko, and the DESERT Group (2005), Thermo-mechanical model of the Dead Sea Transform, *Earth Planet. Sci. Lett.*, *238*, 78–95, doi:10.1016/j.epsl.2005.06.058.

Soto, J. I., F. Fernández-Ibáñez, M. Fernández, and A. García-Casco (2008), Thermal structure of the crust in the Gibraltar Arc: Influence on active tectonics in the western Mediterranean, *Geochem. Geophys. Geosyst.*, *9*, Q10011, doi:10.1029/2008GC002061.

Srivastava, S. P., W. R. Roest, L. C. Kovacs, G. Oakey, S. Levesque, J. Verhoef, and R. Macnab (1990), Motion of Iberia since the Late Jurassic: Results from detailed aeromagnetic measurements in the Newfoundland basin, *Tectonophysics*, *184*, 229–260, doi:10.1016/0040-1951(90)90442-B.

Stern, T., and J. McBride (1998), Seismic exploration of continental strike-slip zones, *Tectonophysics*, *286*, 63–78, doi:10.1016/S0040-1951(97)00255-2.

Van Bemmelen, R. W. (1927), Bijdrage tot de geologie der Betisch Ketens in de provincie Granada, Ph.D. thesis, 176 pp., Univ. of Delft, Delft, Netherlands.

Van de Poel, H. M. (1991), Messinian stratigraphy of the Níjar Basin (S.E. Spain) and the origin of its gypsum-ghost limestones, *Geol. Mijnbouw*, *70*, 215–234.

Weijermars, R., T. B. Roep, B. Van den Eeckhout, G. Postma, and K. Kleverlaan (1985), Uplift history of a Betic fold nappe inferred from Neogene-Quaternary sedimentation and tectonics (in the Sierra Alhamilla and Almería, Sorbas and Tabernas Basins of the Betic Cordilleras, SE Spain), *Geol. Mijnbouw*, *64*, 397–411.

Wessel, P., and W. H. Smith (1998), New improved version of the generic mapping tools released, *Eos Trans. AGU*, *79*, 579, doi:10.1029/98EO00426.

Wight, D. E., and F. X. Bostick (1980), Cascade decimation: A technique for real time estimation of power spectra, paper presented at International Conference on Acoustic, Speech, and Signal Processing, Inst. of Electr. and Electron. Eng., Denver, Colo., 9–11 April.

Wilson, C. K., C. H. Jones, P. Molnar, A. F. Sheehan, and O. S. Boyd (2004), Distributed deformation in the lower crust and upper mantle beneath a continental strike-slip fault zone: Marlborough fault system, South Island, New Zealand, *Geology*, *32*, 837–840, doi:10.1130/G20657.1.

Working Group for Deep Seismic Sounding in the Alboran Sea, 1974 (1978), Crustal seismic profiles in the Alborán Sea preliminary results, *Pure Appl. Geophys.*, *116*, 167–180.

Yoshimura, R., et al. (2009), Magnetotelluric transect of the Niigata-Kobe tectonic zone, central Japan: A clear correlation between strain accumulation and resistivity structure, *Geophys. Res. Lett.*, *36*, L20311, doi:10.1029/2009GL040016.

Zandt, G., and C. J. Ammon (1995), Continental crust composition constrained by measurement of crustal Poisson's ratio, *Nature*, *374*, 152–154, doi:10.1038/374152a0.

Zhu, L. (2002), Deformation in the lower crust and downward extent of the San Andreas Fault as revealed by teleseismic waveforms, *Earth Planets Space*, *54*, 1005–1010.

Zhu, L., and H. Kanamori (2000), Moho depth variation in southern California from teleseismic receiver functions, *J. Geophys. Res.*, *105*, 2969–2980, doi:10.1029/1999JB900322.